


**Optimization induced by stability and the role of limited control near a steady state**J. Gonzalez-Ayala<sup>1,2,\*</sup>, J. Guo,<sup>3,1</sup> A. Medina,<sup>1,2</sup> J. M. M. Roco,<sup>1,2</sup> and A. Calvo Hernández<sup>1,2</sup><sup>1</sup>*Departamento de Física Aplicada, Universidad de Salamanca, 37008 Salamanca, Spain*<sup>2</sup>*Instituto Universitario de Física Fundamental y Matemáticas (IUFFyM), Universidad de Salamanca, 37008 Salamanca, Spain*<sup>3</sup>*College of Physics and Information Engineering, Fuzhou University, Fuzhou 350116, People's Republic of China* (Received 17 May 2019; revised manuscript received 24 September 2019; published 23 December 2019)

A relationship between stability and self-optimization is found for weakly dissipative heat devices. The effect of limited control on operation variables around an steady state is such that, after instabilities, the paths toward relaxation are given by trajectories stemming from restitution forces which improve the system thermodynamic performance (power output, efficiency, and entropy generation). Statistics over random trajectories for many cycles shows this behavior as well. Two types of dynamics are analyzed, one where a stability basin appears and another one where the system is globally stable. Under both dynamics there is an induced trend in the control variables space due to stability. In the energetic space this behavior translates into a preference for better thermodynamic states, and thus stability could favor self-optimization under limited control. This is analyzed from the multiobjective optimization perspective. As a result, the statistical behavior of the system is strongly influenced by the Pareto front (the set of points with the best compromise between several objective functions) and the stability basin. Additionally, endoreversible and irreversible behaviors appear as very relevant limits: The first one is an upper bound in energetic performance, connected with the Pareto front, and the second one represents an attractor for the stochastic trajectories.

DOI: [10.1103/PhysRevE.100.062128](https://doi.org/10.1103/PhysRevE.100.062128)**I. INTRODUCTION**

Regarding heat devices optimization, there is a growing number of papers aiming to approach Carnot efficiency for irreversible heat devices [1–13] and challenging the idea that *you can't have it all*, in other words, the panacea of thermodynamic optimization. Until recently, it was an accepted statement that for heat engines (HE) it was not possible to optimize—simultaneously—power output, efficiency, and entropy production. For this reason, compromise functions among different thermodynamics functions have acquired a major relevance. The present paper is framed within this context.

The initial paradigm of heat devices optimization was the improvement of the efficiency in the conversion of heat into work, mostly in the realm of cyclic reversible and steady-state processes. Later, the development of finite-time thermodynamics brought a second paradigm, the maximum power regime (MP) [14], with the drawback of relying on a number of assumptions on the heat fluxes, dissipation, and considerations on the degree of irreversibility [15–24]. Nowadays, to prove the equivalence of the existing irreversible models is an ongoing subject of research, such is the case, for example, of the low-dissipation model, the linear irreversible model, the irreversible Carnot like model from finite-time thermodynamics, and some more specific cases for stochastic heat engines. More recently, the better use of energy and the impact of energy waste has become a priority and has turned the minimization of entropy into another desirable ingredient

in the optimization. Then, trade-off objective functions (such as the ecological [25], Omega [26], and efficient power [27] functions) came into play [28–32].

Nowadays, the aim to uncover general aspects related to operation regimes, beyond specific models and heat transfer mechanisms, is an active field [33–42]. For this purpose, the analysis of the maximum power regime is the most developed one so far. Of special interest is the so-called Curzon-Ahlborn efficiency [14], until now, a kind of signature of this regime [33,36–38]. Without so much prominence, compromise-based efficiencies such as the so-called ecological and the Omega functions displayed this very same feature in their corresponding efficiencies [34]. Additionally, the knowledge of the influence of control on the operation variables in heat devices remains as an unsolved issue [43]. There are open questions regarding the role of constancy [44] (fluctuations in the energetic output records), which could be lastly related to power fluctuations with large efficiencies in HE's, although subtle differences have been recently reported for quasistatic and steady-state HE models [45]. In this way, issues as the Carnot efficiency at finite power and efficiency at maximum power have been widely analyzed by different strategies to account for control of parameters and engine layouts in macroscopic, mesoscopic, and quantum frameworks [1–12,46–49].

The proposal of dynamics on the optimization variables allowing the departure from the stationary state has recently motivated the search for a possible relation between stability and optimization [50–52]. In view of this evidence, there is a promising way to incorporate stability as a new ingredient in the optimization of HE's with new features appealing for a better understanding of the thermodynamics behind stability,

\*jgonzalezayala@usal.es

which allows to show figures of merit as an emergent property that balances power, entropy and efficiency.

One needs only to look at these, so far, separated components and naturally wonder whether a kind of optimization underlies stability. This is one of the main concerns of the paper. For this purpose local stability will be analyzed at the light of optimization processes in order to unify these two elements, usually considered as separated issues. For weakly dissipative heat devices, it will be shown that they are indeed linked. By means of external perturbations on the control parameters that define the operation regime, a behavior that favors the simultaneous optimization of all the relevant thermodynamic functions is achieved to some extent. Thus, the trajectories toward the steady state constitute an optimization mechanism. This could be useful to face limitations in control and fine-tuning [53–56].

In addition to the possible limitations in the control of the system operation, external fluctuations around the steady state during the cyclic process would induce stochastic trajectories. The analysis of this situation will provide a vision of the statistical consequences of what can be considered as limited control on the operation regime, showing a favorable outcome regarding optimization. To this end, a general model describing weakly dissipative devices is used. Such is the so-called low-dissipation heat engine model [57], which offers a quite straightforward unified heat devices analysis for HE's and refrigerator engines (RE's) [58]. This first-order approach for irreversible deviations from a Carnot cycle makes no use of specific heat transfer mechanisms and focuses instead on the dissipation symmetries in the contact with the hot and cold reservoirs and time constraints. This model constitutes a suitable way to explore general behaviors not linked with particularities in the heat transfer mechanism, with validity in a broad temperature range and including valuable information about possible symmetries [59–63]. An advantage of this model is the capability to reproduce results from a variety of models in the macroscopic and microscopic regime [15,61,63–72].

The present study considers a heat engine described by the low-dissipation model, in which the internal dynamics (including the stochastic nature of the system, if that is the case) is already accounted through some dissipation coefficients. This is more obvious in mesoscopic devices, where the low-dissipation model has gained a greater relevance, however, this could apply to macroscopic systems as well. Once the thermodynamic description is established, the effect of external perturbations on the heat fluxes will be considered under the assumption of a restitution dynamics allowing the system to return to the initial steady state, fixed by the elected operation regime. Possible application of this study could include: (i) a macroscopic solarized irreversible Brayton engine with fluctuations stemming from a wide variety of sources linked to the control variables (see concluding remarks); (ii) a low-dissipation micrometric HE experimentally realized by a single particle in an optical trap through an optical harmonic potential [73,74]; and (iii) a spin vortex confined on a disk with a harmonic potential [75,76]. It is remarkable that the last two systems present a harmonic oscillator confinement potential, which suits well with the stability dynamics used in this work.

In the companion letter [77] the main points on the energetic self-optimization induced by stability have been presented for a dynamic yielding to a unique equilibrium point when the system is perturbed from the stationary state. Here, extended details of these calculations are explicitly given and, beside this, a second and more rich dynamics yielding a basin of attraction is also presented first. The paper is structured as follows. In Sec. II we briefly introduce the model. In Sec. III, in order to have access to a phenomenology linked to endoreversible and irreversible behaviors, one pair of control variables are introduced. The maximum power and maximum Omega regimes are discussed in Sec. III A. In Sec. III B, to provide a general optimization framework and compare it with stability results, the Pareto front is obtained. With this at hand, in Sec. III C, stability in a basin of attraction is addressed for the MP and  $M\Omega$  regimes and the behavior the trajectories to the stable state are studied. In Sec. III D, random consecutive perturbations time are analyzed. In Sec. IV the same procedure is repeated using another pair of control variables which give access to another phenomenology and stability dynamics with a single stable point. In Sec. V some concluding remarks are presented. In Appendix the statistical convergence of the analysis of several trajectories is presented using the Kullback-Leibler divergence.

It is noted that Secs. II and III A contain known results for the low-dissipation model that we include for completeness [50–52]. Additionally, the behavior of trajectories stemming from the stability dynamics due to a single perturbation for the dynamics introduced in Sec. III C were discussed in Ref. [52] but we include them to provide parallel and self-included description of both dynamics.

## II. THE MODEL

Since the Carnot cycle is one of the cornerstones of thermodynamics, it is natural to depart from it for the proposal of describing irreversible devices operating between two thermal reservoirs at constant temperatures  $T_c$  and  $T_h > T_c$ . Irreversibilities are introduced in the contacts between the working fluid and the reservoirs. Under the weakly dissipation hypothesis, the resulting heat engine [57] is described by the contact time of each isothermal process,  $\{t_c, t_h\}$  and the dissipation coefficients  $\{\Sigma_c, \Sigma_h\}$  containing all the intrinsic information about irreversibilities of the fluid and the internal dynamics while in contact with each reservoir. The input and output heats are  $Q_c = -T_c \Delta S (1 + \frac{\Sigma_c}{t_c \Delta S})$  and  $Q_h = T_h \Delta S (1 - \frac{\Sigma_h}{t_h \Delta S})$ , respectively; where  $\Delta S$  is the entropy change at the hot isotherm of the baseline Carnot cycle. The total entropy change is then  $\Delta S_{\text{tot}} = \Sigma_c/t_c + \Sigma_h/t_h$ . The duration of adiabatic processes is neglected. The reversible limit is recovered whenever  $\{t_c, t_h\} \rightarrow \infty$  or  $\{\Sigma_c, \Sigma_h\} \rightarrow 0$ .

The main energetic quantities are the efficiency,  $\eta = (Q_h + Q_c)/Q_h$ ; the power output,  $P = (Q_h + Q_c)/(t_c + t_h)$ ; and entropy production  $\sigma = \Delta S_{\text{tot}}/(t_c + t_h)$ . The  $\Omega$  function is defined as the difference between maximum power gain [ $P_{\text{gain}} = P - P_{\text{min}} = (\eta - \eta_{\text{min}})Q_h$ ] and the minimum power loss [ $P_{\text{loss}} = P_{\text{max}} - P = (\eta_{\text{max}} - \eta)Q_h$ ];  $\Omega \equiv P_{\text{gain}} - P_{\text{loss}}$  [26]. Since the minimum achievable efficiency is 0, and

the maximum is  $\eta_C \equiv 1 - T_c/T_h$ ,

$$\Omega = 2P - P_{\max} - P_{\text{loss}} = (2\eta - \eta_C)\dot{Q}_h, \quad (1)$$

where  $\eta_C = 1 - T_c/T_h$  is the Carnot efficiency. Under these conditions, the  $\Omega$  function is equivalent to the so-called ecological function, a compromise between power output and entropy production, whose mathematical form is  $E = P - T_c\sigma$  [25]. Below, two equivalent optimization variables give rise, nonetheless, to different phenomenologies in the energetic space with the aid of time constraints [50,58]. They give also two different stability behaviors under the assumption that stability is linked with the variation of the control parameters.

### III. TOTAL TIME AND ONE PARTIAL CONTACT TIME AS CONTROL VARIABLES OF THE OPERATION REGIME

The control parameters involved in the operation regime are the contact times with the hot and cold reservoirs,  $t_c$  and  $t_h$ ; however, an interesting phenomenology arises by considering, instead, one contact time and the total cycle time. By defining dimensionless variables that accounts for the system size [60],  $\tilde{\Sigma}_c \equiv \Sigma_c/\Sigma_T$  (and  $\tilde{\Sigma}_h = 1 - \tilde{\Sigma}_c$ ), only one fraction of the total dissipation coefficients is needed,  $\alpha \equiv t_c/(t_c + t_h)$ ,  $\tilde{t} \equiv \Delta S(t_c + t_h)/\Sigma_T$ , with  $\Sigma_T \equiv \Sigma_h + \Sigma_c$  and  $\tau = T_c/T_h$ , and it is possible to introduce dimensionless input and output heats [50],

$$\tilde{Q}_h \equiv \frac{Q_h}{\tilde{t}T_c\Delta S} = \left[1 - \frac{1 - \tilde{\Sigma}_c}{(1 - \alpha)\tilde{t}}\right] \frac{1}{\tau\tilde{t}}, \quad (2)$$

$$\tilde{Q}_c \equiv \frac{Q_c}{\tilde{t}T_c\Delta S} = -\left(1 + \frac{\tilde{\Sigma}_c}{\alpha\tilde{t}}\right) \frac{1}{\tilde{t}}, \quad (3)$$

By scaling according to the size of the baseline Carnot cycle, the characteristic total entropy production, efficiency, power, and the  $\Omega$  function can be obtained [60],

$$\tilde{\sigma} = \frac{1}{\tilde{t}^2} \left( \frac{1 - \tilde{\Sigma}_c}{1 - \alpha} + \frac{\tilde{\Sigma}_c}{\alpha} \right), \quad (4)$$

$$\tilde{\eta} = \eta = 1 - \tau \frac{1 + \frac{\tilde{\Sigma}_c}{\alpha\tilde{t}}}{1 - \frac{1 - \tilde{\Sigma}_c}{(1 - \alpha)\tilde{t}}}, \quad (5)$$

$$\tilde{P} = \frac{1}{\tau\tilde{t}} \left[ 1 - \tau - \frac{1 - \tilde{\Sigma}_c}{(1 - \alpha)\tilde{t}} - \frac{\tau\tilde{\Sigma}_c}{\alpha\tilde{t}} \right], \quad (6)$$

$$\tilde{\Omega} = \frac{1 - \tau}{\tau\tilde{t}} - \frac{(1 + \tau)(1 - \tilde{\Sigma}_c)}{(1 - \alpha)\tilde{t}^2} - \frac{2\tilde{\Sigma}_c}{\alpha\tilde{t}^2}. \quad (7)$$

In this way, all thermodynamic functions,  $f$ , are of the form  $f = f(\tau, \tilde{\Sigma}_c, \alpha, \tilde{t})$ , with  $\tau$  and  $\tilde{\Sigma}_c$  fixed properties of the device and  $\alpha$  and  $\tilde{t}$  the optimization variables. Originally, Esposito *et al.* [57] showed that the optimization variables were the contact times  $t_c$  and  $t_h$ . In Ref. [60],  $\alpha$  and  $\tilde{t}$  were introduced as more suitable independent variables, accounting for the overall system size (through  $\Delta S$ ) and overall dissipation (through  $\Sigma_T$ ). This allows a description of irreversible and endoreversible behaviors from time constraints.

#### A. Maximum power and maximum $\Omega$ regimes

It has been shown that efficiency and entropy production have no global optimum, but under the constraint of fixing the total time, the optimum value with respect to  $\alpha$ , that is,

maximum efficiency ( $M_\eta$ ) and minimum entropy production ( $\tilde{\sigma}_{\min}$ ) can be obtained [62]:

$$\alpha^{\tilde{\sigma}_{\min}} = \frac{1}{1 + \sqrt{\frac{1 - \tilde{\Sigma}_c}{\tilde{\Sigma}_c}}}, \quad (8)$$

$$\alpha^{M_\eta} = \frac{\tilde{\Sigma}_c\tilde{t} - \sqrt{\tilde{\Sigma}_c\tilde{t}(1 - \tilde{\Sigma}_c)(\tilde{t} + 2\tilde{\Sigma}_c - 1)}}{(2\tilde{\Sigma}_c - 1)\tilde{t}}. \quad (9)$$

On the other hand,  $P$  and  $\Omega$  have global maxima, achieved when [62]

$$\alpha^{\text{MP}} = \frac{1}{1 + \sqrt{\frac{1 - \tilde{\Sigma}_c}{\tau\tilde{\Sigma}_c}}}, \quad (10)$$

$$\alpha^{\text{M}\Omega} = \frac{1}{1 + \sqrt{\frac{(1 + \tau)(1 - \tilde{\Sigma}_c)}{2\tau\tilde{\Sigma}_c}}}, \quad (11)$$

and

$$\tilde{t}^{\text{MP}} = \frac{2}{1 - \tau} (\sqrt{\tau\tilde{\Sigma}_c} + \sqrt{1 - \tilde{\Sigma}_c})^2 \quad (12)$$

$$\tilde{t}^{\text{M}\Omega} = \frac{2}{1 - \tau} [\sqrt{2\tau\tilde{\Sigma}_c} + \sqrt{(1 - \tilde{\Sigma}_c)(1 + \tau)}]^2. \quad (13)$$

The resulting efficiencies are monotonically decreasing functions of  $\tilde{\Sigma}_c \in \{0, 1\}$ , bounded by the limits [62]

$$\frac{\eta_C}{2} \leq \eta^{\text{MP}} \leq \frac{\eta_C}{2 - \eta_C}. \quad (14)$$

$$\frac{3\eta_C}{4} \leq \eta^{\text{M}\Omega} \leq \frac{3 - 2\eta_C}{4 - 3\eta_C} \eta_C. \quad (15)$$

If  $\tilde{\Sigma}_c = 1/2$  (dissipation coefficients symmetry), then the Curzon-Ahlborn efficiency,  $\eta_{\text{CA}}$ , and the so-called ecological efficiency,  $\eta_E$ , are obtained [62],

$$\eta^{\text{MP}} = \eta_{\text{CA}} \equiv 1 - \sqrt{\tau}, \quad (16)$$

$$\eta^{\text{M}\Omega} = \eta_E \equiv 1 - \sqrt{\frac{\tau(1 + \tau)}{2}}. \quad (17)$$

Compromise function benefits are summarized in the upper and lower bounds, achieved when  $\tilde{\Sigma}_c \rightarrow \{1, 0\}$  [62],

$$1 \leq \frac{(1 + \tau)^2}{1 + 2\tau} \leq \frac{\tilde{P}^{\text{MP}}}{\tilde{P}^{\text{M}\Omega}} \leq \frac{4}{3}, \quad (18)$$

$$1 \leq (1 + \tau)^2 \leq \frac{\tilde{\Delta S}^{\text{MP}}}{\tilde{\Delta S}^{\text{M}\Omega}} \leq 4, \quad (19)$$

$$\frac{2}{3} \leq \frac{\eta^{\text{MP}}}{\eta^{\text{M}\Omega}} \leq \frac{4 - 3\eta_C}{(2 - \eta_C)(3 - 2\eta_C)} \leq 1, \quad (20)$$

depending on the value of  $\tilde{\Sigma}_c$  significant saving on entropy production and improvement in efficiency can be obtained from small sacrifices of power. For instance, from Eqs. (18)–(20) in a limiting case  $\tilde{\Sigma}_c \rightarrow 0$ , with a similar efficiency and a sacrifice of 1/3th of power output it could be possible to have only 1/4th of the entropy production compared to the MP regime.

A key feature of this representation is the appearance of endoreversible and irreversible behaviors, depending on the time constraints [58]. Endoreversible behavior in finite-time thermodynamics is linked to open  $\eta$ - $P$  parametric curves with

respect to the thermal gradient  $\tau$ . In this case, efficiency is allowed to approach the Carnot limit when the gap between the two external reservoirs tends to zero or the contact times are infinite.

On the other hand, irreversible behaviors are linked to loop-like  $\eta$ - $P$  parametric curves, a signature commonly representative of internal irreversibilities due to all kind of dissipations from the working fluid.

These two behaviors appear from the constraint of fixed  $\alpha$  (being equivalent to the endoreversible hypothesis [70]) and from fixing  $\tilde{t}$  (i.e., fixing the irreversibility of the system). From now on, the two cases will be denoted as the endoreversible and irreversible limits, respectively. They are discussed in detail in Ref. [58], as part of a unified phenomenology for HE's and RE's and will become relevant in the analysis of a stability-optimization relation. Insights on these behaviors from time constraints in the stability and optimization are also discussed for HE's in Ref. [70] and for RE's in Ref. [78].

Since the simultaneous optimization of the most significant energetic functions of the system plays a role in the relaxation trajectories after a perturbation, in the following subsection the multiobjective optimization problem is addressed, providing a standpoint to compare the results stemming from the stability analysis.

**B. The best energetic performance: The Pareto front**

Since there are no configurations fulfilling altogether the maximization of efficiency, power,  $\Omega$ , and entropy minimization, a compromise in the optimization of these quantities should be tackled by means of a multiobjective optimization. This involves the simultaneous maximization or minimization of a number of objective functions [79,80] to obtain the so-called Pareto front, which gives the best compromise among desirable quantities and where a further improvement in one function involves the degrading of the rest.

Two complementary outcomes will be pursued by this analysis: to obtain the Pareto front in the thermodynamic space and its corresponding Pareto optimal set in the time variables space.

Consider the vector  $(\eta, \tilde{P}, \tilde{\sigma}, \tilde{\Omega})$  (the thermodynamic space), the Pareto optimal set comprise the points  $(\alpha, \tilde{t})$ 's (the phase space) for which none of the objectives can be improved without degrading any of the others [79,80], this is known as dominance. The algorithm introduced here is the following:

- (i) In the phase space, the physical region is defined (positive values of power output and efficiency).
- (ii) A random set of points in the phase space is obtained along with its image in the energetic space.
- (iii) With this set of points a provisional Pareto optimal set is found by means of a sorting algorithm based in the concept of dominance [79,80].
- (iv) At this point, a novel technique is introduced to search for new elements in the Pareto front: A convex region containing the provisional Pareto optimal set is computed and expanded in order to cover a larger region to search for new points in the Pareto front. In every iteration the expansion of this region decreases with the value of the Kullback-Leibler divergence [81]. As the statistical information of the Pareto

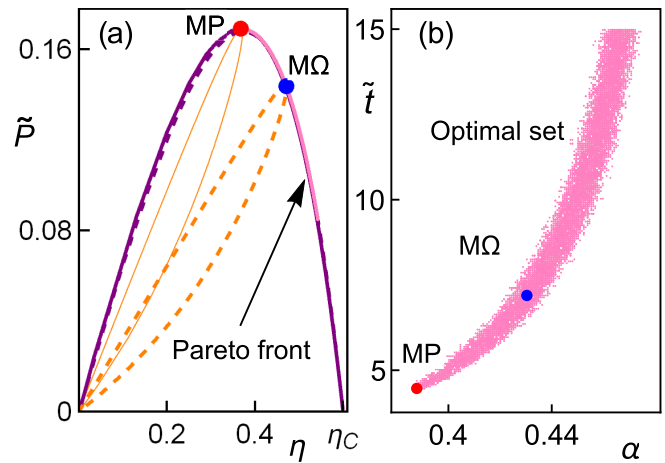


FIG. 1. (a) Endoreversible (parabolic curves, purple online) and irreversible (closed curves, orange online) limits stemming from the constraints  $\alpha = \alpha^{MP}$  and  $\alpha = \alpha^{M\Omega}$ , or  $\tilde{t} = \tilde{t}^{MP}$  and  $\tilde{t} = \tilde{t}^{M\Omega}$ , are represented in solid and dashed curves for the MP and MΩ regimes, respectively. Endoreversible curves are very close to each other. The Pareto front represents an upper bound of the endoreversible limits. In (b) the Pareto optimal set. The Pareto front has been computed for the region  $\tilde{t} \in (0, 15)$ . For values  $\tilde{t} \approx 10^3$  the Pareto front would reach the Carnot efficiency in (a). Here  $\tau = 2/5$  and  $\tilde{\Sigma}_c = 1/2$ .

front converges to a value, this divergence tends to zero and the expansion tends to zero as well. Details on the definition of the expanded region are given in the next paragraph.

(v) From the new region another set of random points in the phase space is proposed and a new provisional Pareto optimal set is found.

The Kullback-Leibler divergence (KLD) [81] is calculated between the distribution of points of the  $i$ th and the  $(i - 1)$ th iterations. The boundary of the convex region in the phase space is expanded with a radii that decreases in every iteration. In the initial iterations it decreases proportionally to  $1/i$ , and from  $i = 5$ , with the KLD value. When this relative entropy is very small there is no information gain in iterating more times, then, the searching for new points in the Pareto optimal set stops.

Figure 1(a) shows the Pareto front with the objective functions  $\tilde{\sigma}$  (minimization),  $\eta$ ,  $\tilde{P}$ , and  $\tilde{\Omega}$  (maximization). Adding compromise functions stemming from  $\tilde{\sigma}$ ,  $\tilde{P}$ , and  $\eta$ , such that  $\Omega$  does not contribute to obtain new points, since they are already contained in the optimal set. Figure 1(a) shows the endoreversible and irreversible limits for both regimes as well. The optimal set forms an envelope for the endoreversible limits (for MP and MΩ); furthermore, it provides an upper boundary for every endoreversible limit of compromise-based functions. The Pareto optimal set is depicted in Fig. 1(b). In these figures  $\tilde{\Sigma}_c = 1/2$ ; thus, the depicted efficiencies correspond to  $\eta_{CA}$ , for MP, and  $\eta_E$  for MΩ [see Eqs. (16) and (17)].

**C. Control and stability**

One of the first concerns when dealing with cyclic processes lies in the ability to maintain an stationary state, which defines an operation regime. Thus, avoiding the system to

evolve far from the desired operation regime is a key point. In this context appears control theory as a tool to provide a way to keep dynamical systems under continuous operation. To achieve this, a corrective behavior is needed, depending on the difference between an actual state and a reference or desired one (a feedback). Although this corrective mechanism is left to external controllers, in the case at hand, the very nature of the weakly dissipative system provides an intrinsic way to come back to the operation state as will be shown later.

The problem of describing stable systems lead the mathematical development of dynamics [82]. This is done in the most simple way through ordinary differential equations. Which in a general framework can be provided by the system  $dx_i/dt = f_i(x_1, \dots, x_n, t)$  with  $i = 1, \dots, n$ . Since the operation regime and further description of the system does not require information on previous states (or the history of the system) there is no need to include explicitly the dependence of time in the last equation, this is known as an autonomous system.

Our interest will remain in the subject of linear systems where all  $x_i$  appear on the right-hand side to the first power only, and no products of  $x_i$ 's appear. State variables ( $\tilde{t}$  and  $\alpha$ ), which define the operation regime, will be represented as functions of time (dynamical time); leading in a natural way to the time-domain approach, justifying the use of first-order differential equations. Since the phase space involves two variables, the analysis is restricted to a two-dimensional system (a second-order system).

If one defines  $x_1 = \alpha - \alpha^*$  and  $x_2 = \tilde{t} - \tilde{t}^*$ , then the second-order system above mentioned will have one fixed point at  $(x_1, x_2) = (0, 0)$ , meaning the point  $(\alpha^*, \tilde{t}^*)$  in the phase space. In this case  $d\alpha/dt = 0$  and  $d\tilde{t}/dt = 0$ , corresponding to an equilibrium solution (also called steady state or constant or rest solution) since the systems will remain in that state for further times.

#### D. Stability dynamics

Time variables are associated with heat fluxes between the system and the heat reservoirs. If the system intrinsic properties and external thermal baths are unaltered, then to keep  $\{\Sigma_c, \Sigma_h\}$  unchanged is reasonable. This makes plausible to link external perturbations as variations of the operation times, affecting the energy fluxes. Notice that these perturbations come from external sources and are not linked to the internal dynamics, already accounted by the coefficients  $\tilde{\Sigma}_{c,h}$ .

It is assumed that the system has an equilibrium point at the operation regime. With no further information regarding the specific energy transport,  $\tilde{t}$  and  $\alpha$  are assumed to follow, within the first-order scheme [82], typical relations for an autonomous system. Within the first-order scheme, a typical (and the simplest) relation for an autonomous system in one dimension is given by a dynamical equation  $\dot{x} = -Ax$ , which mimics the restitution force of a harmonic oscillator, a good approximation near a stable point. For the present two-dimensional case, the generalization of the above dynamical equation [82] will be given by

$$\dot{\mathcal{X}} = -\mathbb{A} \mathcal{X}, \quad (21)$$

where  $\mathcal{X} = (\alpha - \alpha^*, \tilde{t} - \tilde{t}^*)$ ,  $\dot{\mathcal{X}} = d\mathcal{X}/dt$  with  $t$  a dynamical dimensionless time with a characteristic timescale to be chosen later, and  $\mathbb{A} \in M_{2 \times 2}$ .

Before introducing in the last expression the roles of heat and power output, *a priori* consideration to understand this linking is that for the time variable  $\alpha$ ,  $\tilde{Q}_c$  would be the natural energy flux associated (variations of  $\alpha$  will produce changes in the output heat). Meanwhile for  $\tilde{t}$ , its associated energy flux will be  $\tilde{P}$ , so that variations on the total time affect the power output.

From a first-order expansion of  $\tilde{Q}_c$  and  $\tilde{P}$  around the steady state one obtains

$$\begin{bmatrix} \tilde{Q}_c(\alpha, \tilde{t}) - \tilde{Q}_c(\alpha^*, \tilde{t}^*) \\ \tilde{P}(\alpha, \tilde{t}) - \tilde{P}(\alpha^*, \tilde{t}^*) \end{bmatrix} = \mathcal{J} \begin{bmatrix} \alpha - \alpha^* \\ \tilde{t} - \tilde{t}^* \end{bmatrix}, \quad (22)$$

with  $\mathcal{J}$  the Jacobian matrix

$$\mathcal{J} = \begin{bmatrix} \left. \frac{d\tilde{Q}_c(\alpha, \tilde{t})}{d\alpha} \right|_{\alpha^*, \tilde{t}^*} & \left. \frac{d\tilde{Q}_c(\alpha, \tilde{t})}{d\tilde{t}} \right|_{\alpha^*, \tilde{t}^*} \\ \left. \frac{d\tilde{P}(\alpha, \tilde{t})}{d\alpha} \right|_{\alpha^*, \tilde{t}^*} & \left. \frac{d\tilde{P}(\alpha, \tilde{t})}{d\tilde{t}} \right|_{\alpha^*, \tilde{t}^*} \end{bmatrix}. \quad (23)$$

Then, as long as the perturbations in  $\tilde{Q}_c$  and  $\tilde{P}$  are small, the linear system in Eq. (21) can be written as

$$\frac{d\alpha}{dt} = C[\tilde{Q}_c(\alpha^*, \tilde{t}^*) - \tilde{Q}_c(\alpha, \tilde{t})], \quad (24)$$

$$\frac{d\tilde{t}}{dt} = D[\tilde{P}(\alpha^*, \tilde{t}^*) - \tilde{P}(\alpha, \tilde{t})], \quad (25)$$

where  $\mathbb{A} = -\begin{bmatrix} C & 0 \\ 0 & D \end{bmatrix} \mathcal{J}$ ;  $C$  and  $D$  are positive constants determining the response speed to perturbations from the steady state that we will refer as the restitution strength [50–52]. Their values may depend on multiple characteristics, but usually the system size is the most important. Because large systems are more likely to respond slowly to perturbations on the control variables than small systems, the larger the system the smaller the values of  $C$  and  $D$ . From a dynamical perspective, their inverse values set a characteristic timescale, so that large values of  $C$  and  $D$  correspond to large restitution strength and short characteristic times. In the forthcoming analyses, results are referred to this timescale.

In the linear approximation, steady-state local stability is determined by  $\mathbb{A}$

$$\mathbb{A} = - \begin{bmatrix} C \left. \frac{\partial \tilde{Q}_c}{\partial \alpha} \right|_{\alpha^*, \tilde{t}^*} & C \left. \frac{\partial \tilde{Q}_c}{\partial \tilde{t}} \right|_{\alpha^*, \tilde{t}^*} \\ D \left. \frac{\partial \tilde{P}}{\partial \alpha} \right|_{\alpha^*, \tilde{t}^*} & D \left. \frac{\partial \tilde{P}}{\partial \tilde{t}} \right|_{\alpha^*, \tilde{t}^*} \end{bmatrix}. \quad (26)$$

The second row in the MP regime is zero, and for the  $M\Omega$  regime is a linear combination of the first row; thus, the determinant of  $\mathbb{A}$  is zero and there is only one eigenvalue corresponding to  $\lambda_1 = C \partial \tilde{Q}_c / \partial \alpha |_{\alpha^*, \tilde{t}^*}$  and stability is described through the evolution of  $\alpha$ , having an infinite set of fixed points, from which only  $\alpha^*$ ,  $\tilde{t}^*$  correspond to the operation regime. This forms the so-called nullcline of  $\alpha$ . Its geometrical space  $[\tilde{t}_{\text{nullcline}}(\alpha, \Sigma_c, \tau)]$  can be obtained from solving  $\partial \alpha / \partial \tilde{t} = 0$ . This curve plays an important role on the statistical behavior of the system, being an attractor on the evolution of the system under continuous perturbations, as will be shown.

Relaxation time in each regime is given by  $t_{\text{relax}} \equiv \lambda_1^{-1}$ ,

$$t_{\text{relax}}^{\text{MP}} = \frac{2(1 - \eta_C)}{C \eta_C} \tilde{t}^{\text{MP}}, \quad (27)$$

$$t_{\text{relax}}^{\text{M}\Omega} = \frac{4(1 - \eta_C)}{C' \eta_C} \tilde{t}^{\text{M}\Omega}, \quad (28)$$

where  $C$  and  $C'$  are used to distinguish between the constant in Eq. (24) in the MP and the  $\text{M}\Omega$  regimes. This result is relevant for our analysis since it relates two timescales, one linked with stability, given by  $t_{\text{relax}}$ , and the other linked with optimization,  $\tilde{t}$ . Moreover, in a cyclic process it would be required to impose the constraint  $t_{\text{relax}} \leq \tilde{t}$ , which determines the restitution strength by means of the constants  $C$  and  $C'$ , fulfilling that

$$C \geq C^{\text{MP}} = \frac{2(1 - \eta_C)}{\eta_C}, \quad (29)$$

$$C' \geq C^{\text{M}\Omega} = \frac{4(1 - \eta_C)}{\eta_C}. \quad (30)$$

Although  $D$  is not involved in these constraints, it affects the basin shape, which also depends on  $\tau$  and  $\tilde{\Sigma}_c$ . Considering  $D$  larger (smaller) than  $C$  produces narrower (wider) stability basins in the  $\tilde{t}$  direction.

The system given by Eqs. (24) and (25) can be solved numerically for the whole dynamics. Representative trajectories stemming from the numerical solution of the dynamic equations with initial points in which  $\alpha$  is small are depicted in Fig. 2 for the MP and  $\text{M}\Omega$  regimes. Perturbations driving the system into the basin of attraction produce trajectories leading to the steady state (red curves), meanwhile perturbations outward (blue curves) lead to a nonphysical state where  $P \leq 0$ . All blue trajectories approach to the shaded region depicted in Fig. 2. Dashed blue lines arrive from the left to this diverging trajectory and solid lines surround the stability basin. The nullcline using Eqs. (24) and (25) is shown for each regime. Additionally, the constraints of constant  $\alpha$  and  $\tilde{t}$  with  $\alpha = \alpha^{\text{MP}}$  (or  $\alpha^{\text{M}\Omega}$ ) corresponding to vertical lines and  $\tilde{t} = \tilde{t}^{\text{MP}}$  (or  $\tilde{t}^{\text{M}\Omega}$ ) corresponding to horizontal lines lead to irreversible and endoreversible behaviors (see orange looplike and purple parabolic-like curves in Fig. 1, respectively). Note that these constraints yield to trajectories crossing at the steady state.

Figure 3 shows the representative trajectories displayed in Fig. 2 in the phase space but in the energetic space accounted for  $\eta$ ,  $\tilde{P}$ ,  $\tilde{\sigma}$ . Notice that far from the steady state, trajectories tend to reach the endoreversible limit by improving simultaneously all the energetic functions  $\eta$ ,  $P$ , and  $\sigma$ . Later, one or more energetic functions have to compromise; however, red curves have the smallest drops and arrive to the steady state in a decaying trajectory bounded by the irreversible limit. The endoreversible limit acts as an attractor involved in an energetic self-improvement of the system, meanwhile the irreversible limit bounds the basin of attraction. The nullcline is shown as well. Arrows point out, in dynamic trajectories, to the forward direction in dynamic time; in the endoreversible limit, the increasing of  $\tilde{t}$ ; in the irreversible limit and the nullcline, the increasing of  $\alpha$ . A black point over the irreversible curve indicates the minimum entropy production state, which [see Fig. 3(c)] does not correspond to the maximum efficiency. The nullcline seems very close to

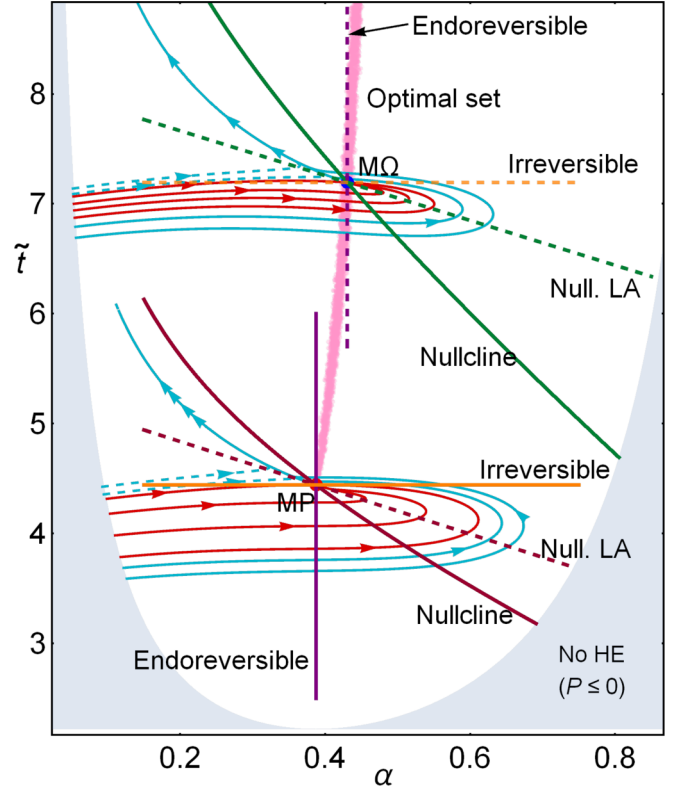


FIG. 2. Basins of attraction for MP and  $\text{M}\Omega$ . Trajectories inside (red online) evolve to the steady state and the rest (blue online) to  $\alpha \rightarrow 0$ ,  $\tilde{t} \rightarrow \infty$ , and  $P \rightarrow 0$ . The nullcline of the dynamics is depicted for each regime. The Pareto optimal set is depicted as well. For each regime, their endoreversible (vertical lines) and irreversible (horizontal lines) limits are shown in solid lines for MP and in dashed lines for the  $\text{M}\Omega$  regime.  $\tau = 2/5$  and  $\tilde{\Sigma}_c = 1/2$  are used. In both regimes the representative case  $C = D = C^{\text{MP}}$  (or  $C^{\text{M}\Omega}$ ) is presented, although the qualitative behavior is the same for other values.

the irreversible limit. Analog results are obtained for the  $\text{M}\Omega$  regime [see Figs. 3(d)–3(f)].

### E. Random perturbations and Markovian cycle to cycle performance

When the precision on the control variables is not enough, fluctuations due to random perturbations around the steady state are expected and in the *cyclic process* the system undergoes stochastic trajectories. Below it is assumed the evolution of the system under consecutive random perturbations. This provides a vision of the statistical consequences of stability under limited control on the operation regime and what could be considered as a disadvantage (at first glance) might result instead in a favorable outcome regarding optimization. Notice that these perturbations might well come from external sources to the system.

A simple model for consecutive perturbations can be accomplished by considering a large number,  $N$ , of perturbations equally distributed in time along one cycle in subintervals of length  $\Delta t$ . The state after each step is computed by solving the stochastic differential equation (SDE) based on the

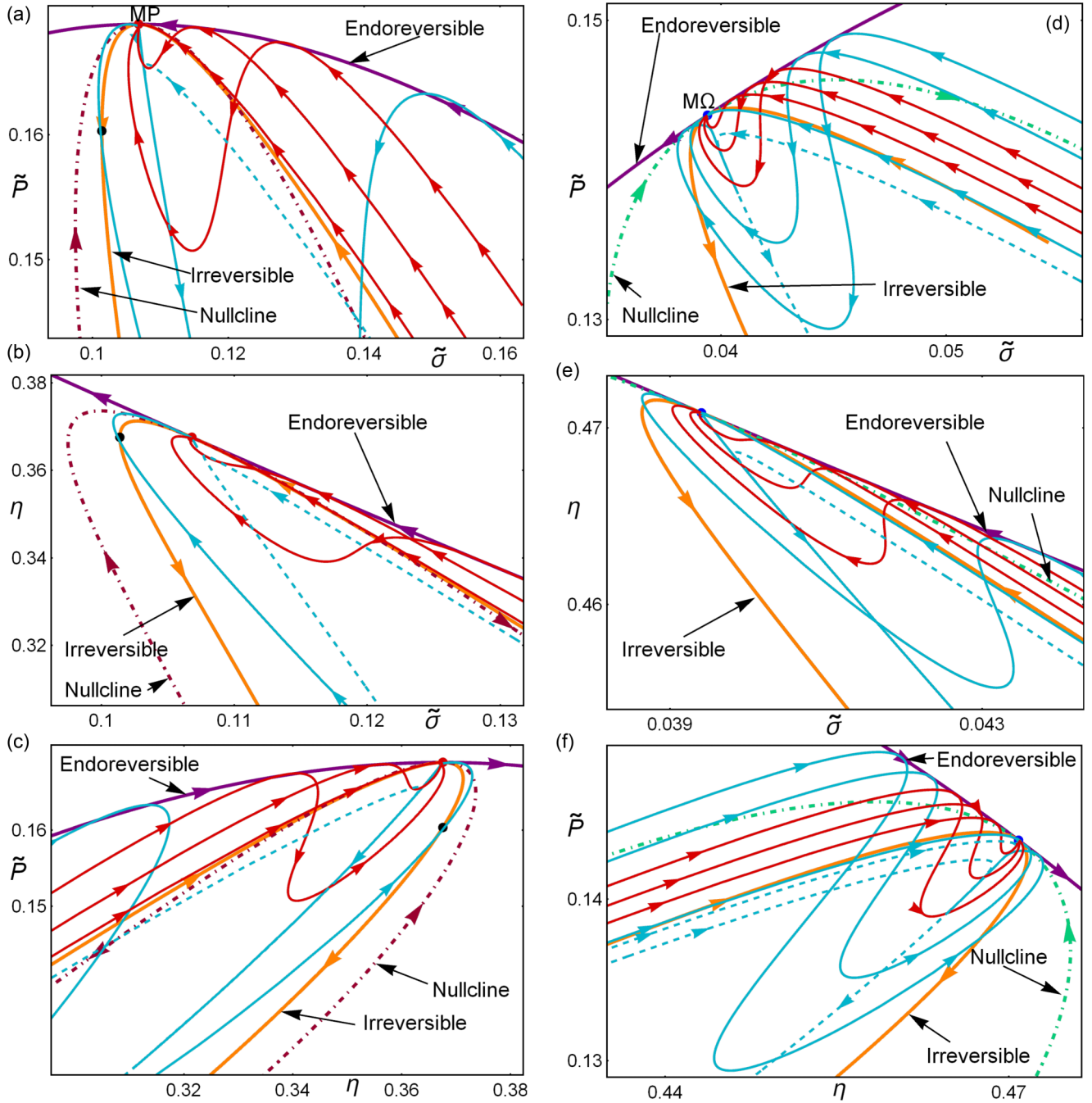


FIG. 3. Relaxation trajectories for the MP case. Endoreversible (purple) and irreversible (orange) limits are depicted, as well as the nullcline of the whole dynamics (siena). In (a) relaxation trajectories in the  $(\tilde{P}, \tilde{\sigma})$  plane. In (b) the same trajectories but in the  $(\eta, \tilde{\sigma})$  plane and in (c) in the  $(\tilde{P}, \eta)$  plane. As in Fig. 1, blue lines are for trajectories outside the stability basin, from which solid lines round the stability basin; meanwhile, dashed lines arrive directly to the diverging trajectory. Red trajectories arrive to the steady state. In all figures  $t_{\text{relax}}^{\text{MP}} = \tilde{t}^{\text{MP}}$ ,  $\tau = 2/5$ , and  $\tilde{\Sigma}_c = 1/2$ . The red point indicates the MP state and the black point the  $\tilde{\sigma}_{\text{min}}$  state with the constraint  $\tilde{t} = \tilde{t}^{\text{MP}}$ . In (d)–(f) the corresponding relaxation trajectories for the  $M\Omega$  regime are presented. Their behavior is qualitatively the same than in the MP case. Far from the steady state, trajectories head to the endoreversible limit with increasing  $\tilde{P}$ , decreasing  $\tilde{\sigma}$ , and increasing  $\eta$ , a simultaneous optimization of the most relevant functions. After arriving to the endoreversible curve those evolving to the steady state are bounded by the irreversible curve. The nullcline of the whole dynamics is depicted in dot-dashed line (green online). In these figures  $t_{\text{relax}} = \tilde{t}^{M\Omega}$  with the representative case  $C = D = C^{\text{MP}}$  (or  $C^{M\Omega}$ ). Note that all the depicted curves lie in two-dimensional manifold in the  $\tilde{P}$ - $\eta$ - $\tilde{\sigma}$  space. The relaxation trajectories are similar to those shown in Figs. 4 and 5 of Ref. [52].

proposed stability dynamics [Eqs. (24) and (25)]. By means of a normally distributed random variable as an additive white noise, the SDE can be solved through the Euler-Maruyama method [83]. The points in the phase space are computed by iterating

$$\Delta\alpha_i = C[\tilde{Q}_c(\alpha^*, \tilde{t}^*) - \tilde{Q}_c(\alpha_i, \tilde{t}_i)]\Delta t + \xi_1\sqrt{\Delta t}, \quad (31)$$

$$\Delta\tilde{t}_i = D[\tilde{P}(\alpha^*, \tilde{t}^*) - \tilde{P}(\alpha_i, \tilde{t}_i)]\Delta t + \xi_2\sqrt{\Delta t}, \quad (32)$$

where the independent stochastic variables  $\{\xi_1, \xi_2\}$  in the  $\alpha$ - $\tilde{t}$  directions obey a two-dimensional Gaussian distribution,

$$f_{\xi}(\tilde{t}_c, \tilde{t}_h) = \frac{\beta^2}{2\pi\alpha^*\tilde{t}^*} e^{-\beta^2[(\frac{\alpha}{\alpha^*})^2 + (\frac{\tilde{t}}{\tilde{t}^*})^2]}, \quad (33)$$

where  $\beta$  is such that standard deviations are proportional to the control variables,  $\sigma_{\tilde{t}} = \tilde{t}/\beta$  and  $\sigma_{\alpha} = \alpha/\beta$ . It is important to highlight that  $t$  (and for extension  $\Delta t$ ) in above equations for the stochastic dynamics is different from  $\tilde{t}$ , which refers to the operation (thermodynamic) time. However, both of them are bounded by the relaxation time  $t_{\text{relax}}$ , which, as stated above, fixes the restitution strengths given by  $C$  and  $D$ .

Trajectories for a complete cycle ( $10^4$  steps) for the MP regime, considering  $(\alpha_1, \tilde{t}_1) = (\alpha^{\text{MP}}, \tilde{t}^{\text{MP}})$  with  $\Delta t$  a  $10^{-4}$ th of a cycle period  $\tilde{t}^{\text{MP}}$  are obtained from (31) and (32). Due to the random nature of these external perturbations one might expect that the system run away from the fixed point. However (see below), the size of the perturbations is such that even for extended periods of time, the system will remain close to the stable state.

For each trajectory final and average states for  $\tilde{P}$ ,  $\eta$ ,  $\tilde{\Omega}$ , and  $\tilde{\sigma}$  are computed. This is repeated for  $10^5$  cycles. After  $10^5$  trajectories or cycles, an statistical convergence is accomplished according to the relative entropy given by the Kullback-Leibler divergence (Appendix). The results are presented in Fig. 4(a), distinguishing points ending inside (green) and outside (blue) of the stability basin to determine the distinctive behaviors. The nullcline is an attractor in each stochastic trajectory. Statistically, its relevance can be seen from Fig. 4, showing that the final states locus are located around it.

For each trajectory average values of the thermodynamic functions are calculated, which are depicted in Fig. 4(b). In comparison with the steady-state values, the cases ending outside the basin of attraction have larger  $\Omega$  values and efficiencies, as well as smaller entropy production. The opposite occurs with green points. Also, the number of cases inside the attraction basin is larger than those outside. In Fig. 4(c) the corresponding probability distribution functions for  $\tilde{\Omega}$ ,  $\eta$ , and  $\tilde{\sigma}$  show the distinctive behavior, with averages displaced from the center and with different heights. In Figs. 4(d)–4(f) the same information for  $\text{M}\Omega$  is also shown.

In Fig. 5(a), final states after each cycle are displayed in the  $\tilde{P}$ - $\eta$ - $\tilde{\sigma}$  space. The endoreversible limit establishes an upper bound for all configurations, which are located around the irreversible limit. It is not guaranteed that the final states will reflect the average behavior of the system. For this reason in Fig. 5(b) the averaged states in each cycle are depicted. Finally, in Fig. 5(c) the averaged states are depicted. The performance of the  $10^5$  cycles is very close to the irreversible behavior. A similar analysis is made for the  $\text{M}\Omega$  regime,

having the same behavior, which is depicted in Figs. 5(d)–5(f). Here, once more, the attracting role of the nullcline is visible.

These results reinforce the idea that the endoreversible limit represents an upper bound for the energetic performance, being an attractor involved in the simultaneous improvement of energetic functions. The irreversible limit discriminates trajectories converging to the steady state, affecting also the overall statistical behavior of many trajectories. Near the steady state, trajectories that cross the irreversible limit (see yellow curve in Fig. 3) will not converge to the steady state but to a decaying trajectory toward  $\tilde{P} \rightarrow 0$ , as discussed in Ref. [52].

#### IV. PARTIAL CONTACT TIMES AS CONTROL VARIABLES OF THE OPERATION REGIME

Another description of the weakly dissipative heat engine is achieved by means of the dimensionless variables  $\tilde{t}_c \equiv t_c \Delta S / \Sigma_h$ ,  $\tilde{t}_h \equiv t_h \Delta S / \Sigma_h$ , that account for the system size, and  $\Sigma \equiv \Sigma_c / \Sigma_h$ . It is easy from these variables to express in a dimensionless way the most relevant thermodynamic functions for heat engines,

$$\tilde{Q}_c = -\tau \left(1 + \frac{\Sigma}{\tilde{t}_c}\right), \quad \tilde{Q}_h = -\left(1 - \frac{1}{\tilde{t}_h}\right), \quad (34)$$

where  $\tilde{Q}_c \equiv Q_c / (T_h \Delta S)$  and  $\tilde{Q}_h \equiv Q_h / (T_h \Delta S)$ , with  $\tilde{\sigma} \equiv \sigma / \Delta S = \tilde{t}_h^{-1} + \Sigma \tau \tilde{t}_c^{-1}$  and

$$\tilde{\eta} = \eta = \frac{1 - \tau - \frac{1}{\tilde{t}_h} - \frac{\tau \Sigma}{\tilde{t}_c}}{1 - \frac{1}{\tilde{t}_h}}, \quad (35)$$

$$\tilde{P} \equiv \frac{P}{T_h \Delta S} = \frac{1 - \tau - \frac{1}{\tilde{t}_h} - \frac{\tau \Sigma}{\tilde{t}_c}}{t_c + t_h}, \quad (36)$$

$$\tilde{\Omega} \equiv \frac{\Omega}{T_h \Delta S} = \frac{1 - \tau - \frac{1}{\tilde{t}_h} - \frac{2\tau \Sigma}{\tilde{t}_c}}{\tilde{t}_h + \tilde{t}_c}. \quad (37)$$

Except for the heats, all the above thermodynamic functions are of the form  $f = f(\tau, \Sigma, \tilde{t}_c, \tilde{t}_h)$ , where  $\tau$  and  $\Sigma$  are fixed properties of the device and  $\{\tilde{t}_c, \tilde{t}_h\}$  are the optimization variables. There are no global maxima for  $\eta$  and  $\tilde{\sigma}$ , but there are maxima for  $\tilde{P}$  and  $\tilde{\Omega}$ ,

$$\tilde{t}_c^{\text{MP}} = \frac{2\tau \Sigma}{1 - \tau} \left(1 + \frac{1}{\sqrt{\tau \Sigma}}\right), \quad (38)$$

$$\tilde{t}_h^{\text{MP}} = \frac{2}{1 - \tau} (1 + \sqrt{\tau \Sigma}), \quad (39)$$

$$\tilde{t}_c^{\text{M}\Omega} = \frac{4\tau \Sigma}{1 - \tau} \left(1 + \frac{1 + \tau}{\sqrt{2\tau \Sigma}}\right), \quad (40)$$

$$\tilde{t}_h^{\text{M}\Omega} = \frac{2(1 + \tau)}{1 - \tau} \left(1 + \sqrt{\frac{2\tau \Sigma}{1 + \tau}}\right). \quad (41)$$

The resulting efficiencies are monotonically decreasing functions of  $\Sigma$ , bounded by  $\Sigma \rightarrow \{\infty, 0\}$ , in agreement with Eqs. (14) and (15), reproducing the symmetric cases  $\Sigma = 1$  [see Eqs. (16) and (17)]. Total operation times are

$$\tilde{t}_{\text{tot}}^{\text{MP}} \equiv \tilde{t}_c^{\text{MP}} + \tilde{t}_h^{\text{MP}} = \frac{2}{\eta c} [1 + \sqrt{(1 - \eta c)\Sigma}]^2, \quad (42)$$

$$\tilde{t}_{\text{tot}}^{\text{M}\Omega} \equiv \tilde{t}_c^{\text{M}\Omega} + \tilde{t}_h^{\text{M}\Omega} = \frac{2(2 - \eta c)}{\eta c} \left[1 + \sqrt{\frac{(1 - \eta c)\Sigma}{2 - \eta c}}\right]^2. \quad (43)$$

The multiobjective optimization is addressed below.



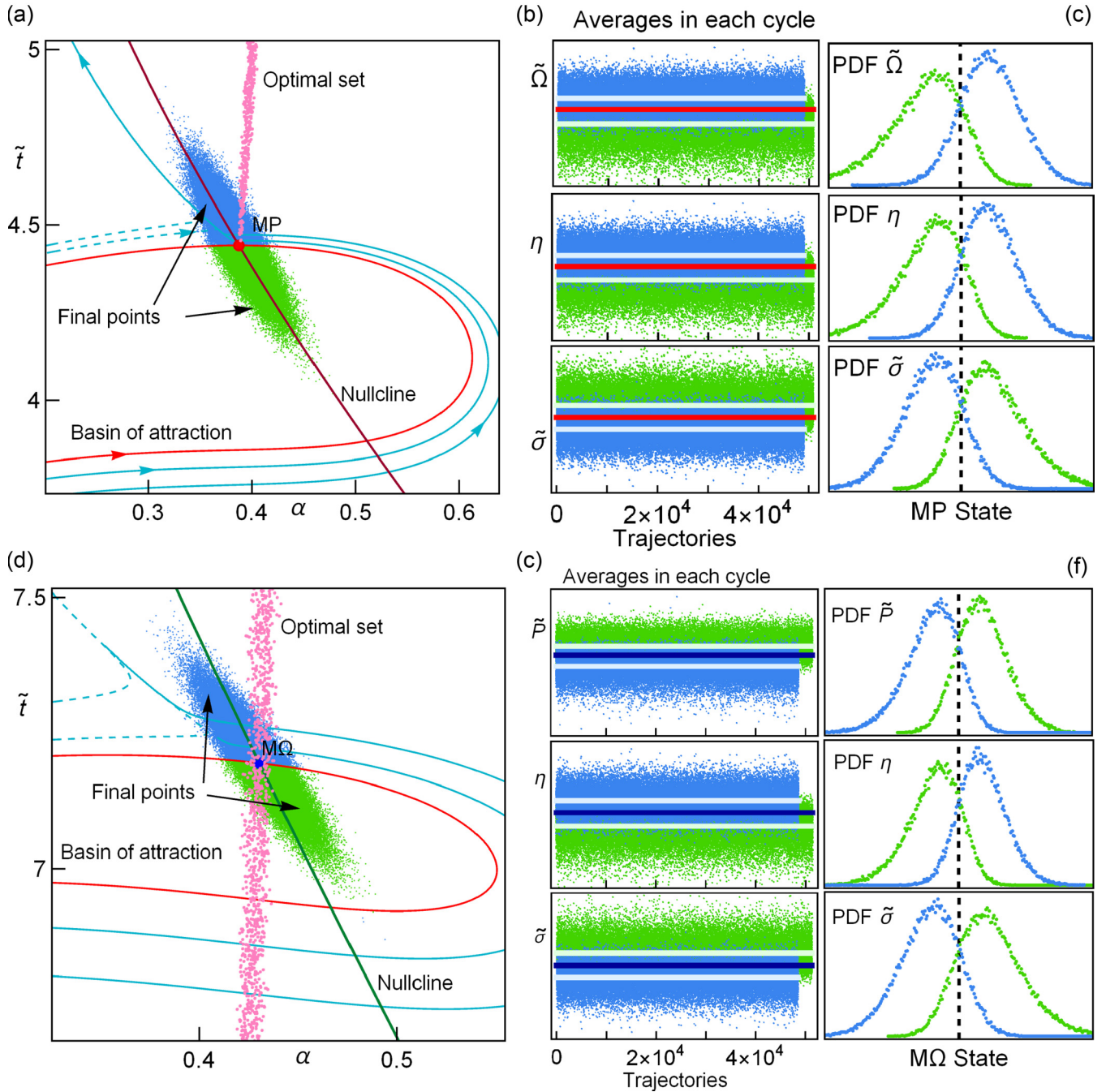


FIG. 4. (a) Final states after  $10^4$  perturbations in one cycle are depicted for  $10^5$  cycles. In blue, states outside the stable region and in green those inside the stable region. Slightly more points are found inside the stability region. Standard deviations of perturbations are  $\{\sigma_\alpha, \sigma_{\tilde{t}}\} = \{\alpha^{\text{M}\Omega}/100, \tilde{t}^{\text{M}\Omega}/100\}$ ;  $t_{\text{relax}}^{\text{MP}} = \tilde{t}^{\text{MP}}$  and  $C = D$ , the values  $\tau = 2/5$  and  $\tilde{\Sigma}_c = 1/2$  are used. In (b) average values of  $\tilde{\Omega}$ ,  $\eta$ , and  $\tilde{\sigma}$  for each cycle. The mean values for all trajectories inside and outside are depicted as horizontal lines (light green and light blue online), and the horizontal line in between (red online) corresponds to the MP state. In (c) the probability distribution function (PDF) for the same energetic functions. It is considered the commonly used square-root criterion [84] for choosing the number of bins or intervals to compute the distribution function, resulting in  $\sqrt{10^5}$  equal intervals. In (d)–(f) the same is reproduced for the MΩ regime. The perturbations in this case are smaller than in the MP case:  $\{\sigma_\alpha, \sigma_{\tilde{t}}\} = \{\alpha^{\text{M}\Omega} \Delta t/100\sqrt{10}, \tilde{t}^{\text{M}\Omega} \Delta t/100\sqrt{10}\}$ . The relaxation time considered is  $t_{\text{relax}} = \tilde{t}^{\text{M}\Omega}$ .

#### A. The best energetic performance: The Pareto front

The algorithm introduced in Sec. III B is used and the corresponding results are displayed in Fig. 6. The optimized functions are  $\tilde{P}$ ,  $\eta$ ,  $\tilde{\Omega}$ , and  $\tilde{\sigma}$ .

In Fig. 6 the optimal set and the Pareto front are displayed. The endoreversible and irreversible limits appearing in the

first set of variables (corresponding to curves of constant  $\tilde{t}$  and  $\alpha$ , respectively) are depicted in the  $\tilde{t}_c, \tilde{t}_h$  space [see the straight lines depicted in Fig. 6(a)].

As expected, the Pareto front is near the endoreversible limit passing by the MP and MΩ states [see Fig. 6(b)]. This zone is close to the endoreversible curves and contains the two

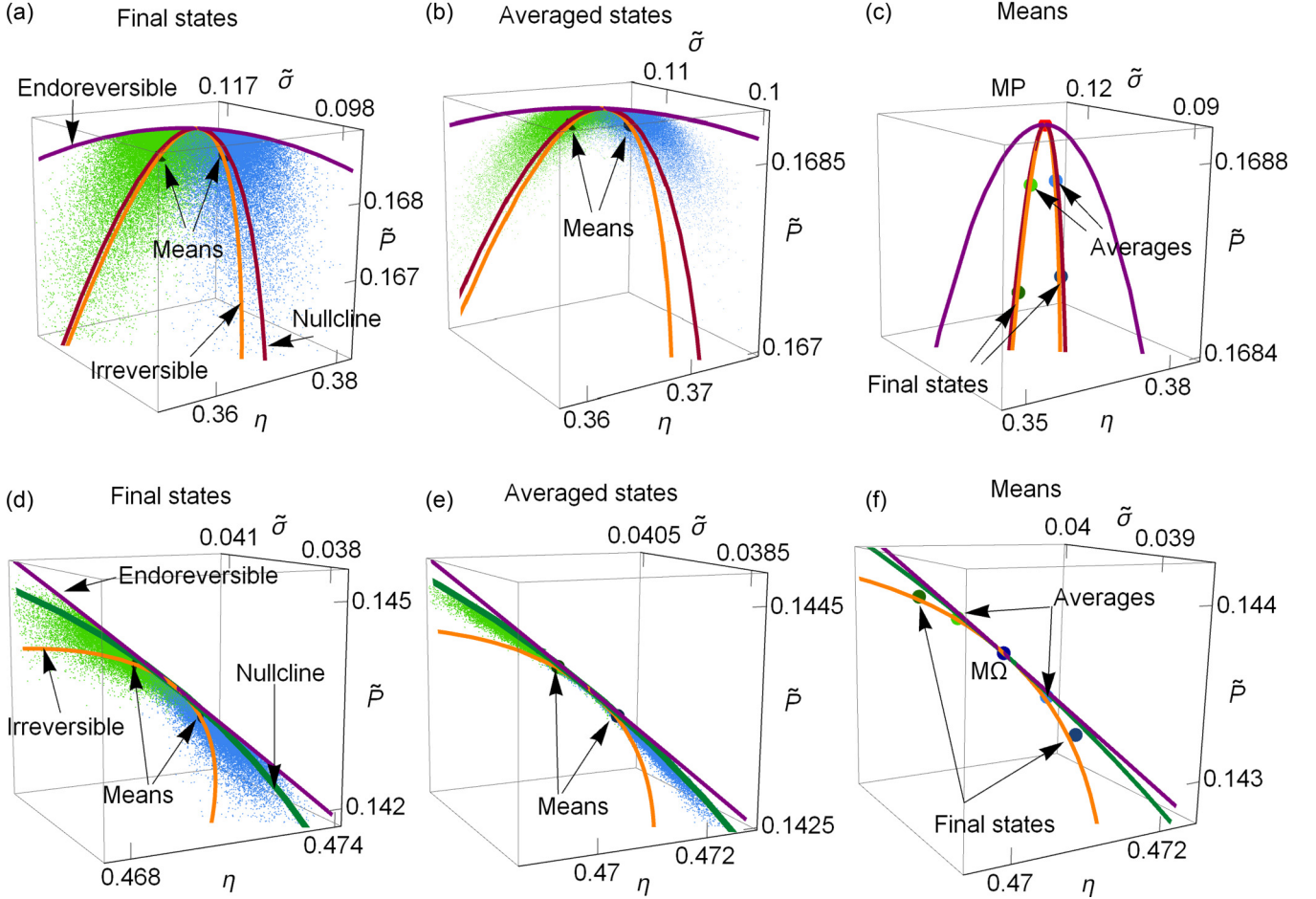


FIG. 5. In (a)  $\tilde{P}$ ,  $\eta$ , and  $\tilde{\sigma}$  of the final states for the  $10^5$  trajectories depicted in Fig. 4, along with the mean value for trajectories inside or outside the basin of attraction. In (b) the averaged values of each trajectory are displayed along with their mean values. In (c) the means displayed in (a) and (b). Notice that they are very close to the irreversible limit (orange online) and close to the nullcline (dark magenta online). In (d)–(f) the corresponding trajectories around the  $M\Omega$  steady state. All points, nullclines, and irreversible or reversible curves lie on a two-dimensional manifold. Notice that they are closer to the nullcline (darker cyan) than to the irreversible limit (orange). Representative values of  $\tau = 2/5$  and  $\tilde{\Sigma}_c = 1/2$  are used.

endoreversible curves. Endoreversible and irreversible curves are depicted in solid lines for the MP regime and in dashed lines for the  $M\Omega$  regime.

**B. Stability dynamics**

Similarly to the previous dynamics, let us assume that the operation regime corresponds to an equilibrium state given by  $\tilde{t}_c^*$  and  $\tilde{t}_h^*$ . For fixed  $\tau$  and  $\Sigma$  (intrinsic properties of the system) perturbations to the steady state arise solely from variations on the operation times. Each heat only depends on the associated partial contact time, i.e.,  $\tilde{Q}_c = \tilde{Q}_c(\tilde{t}_c)$  and  $\tilde{Q}_h = \tilde{Q}_h(\tilde{t}_h)$  [see Eq. (34)], and then variations on the contact times can be effectively linked to variations on the corresponding input or output heats. The matrix formulation given in the previous section can now be addressed as a first-order one-dimensional uncoupled system [82]. The autonomous equations for the dynamics now have the form

$$\frac{d}{dt}(\tilde{t}_c - \tilde{t}_c^*) \propto -(\tilde{t}_c - \tilde{t}_c^*), \tag{44}$$

$$\frac{d}{dt}(\tilde{t}_h - \tilde{t}_h^*) \propto -(\tilde{t}_h - \tilde{t}_h^*). \tag{45}$$

On the other hand, the first-order expansion of  $\tilde{Q}_c$  and  $\tilde{Q}_h$  around the steady state gives

$$\tilde{Q}_c(\tilde{t}_c) - \tilde{Q}_c(\tilde{t}_c^*) = \left. \frac{d\tilde{Q}_c(\tilde{t}_c)}{d\tilde{t}_c} \right|_{\tilde{t}_c^*} (\tilde{t}_c - \tilde{t}_c^*), \tag{46}$$

$$\tilde{Q}_h(\tilde{t}_h) - \tilde{Q}_h(\tilde{t}_h^*) = \left. \frac{d\tilde{Q}_h(\tilde{t}_h)}{d\tilde{t}_h} \right|_{\tilde{t}_h^*} (\tilde{t}_h - \tilde{t}_h^*). \tag{47}$$

By combining Eqs. (44)–(47), it is possible to provide a dynamics linking the contact times with variations in the input and output heats as follows:

$$\frac{d\tilde{t}_c}{dt} = A[\tilde{Q}_c(\tilde{t}_c^*) - \tilde{Q}_c(\tilde{t}_c)], \tag{48}$$

$$\frac{d\tilde{t}_h}{dt} = B[\tilde{Q}_h(\tilde{t}_h^*) - \tilde{Q}_h(\tilde{t}_h)], \tag{49}$$

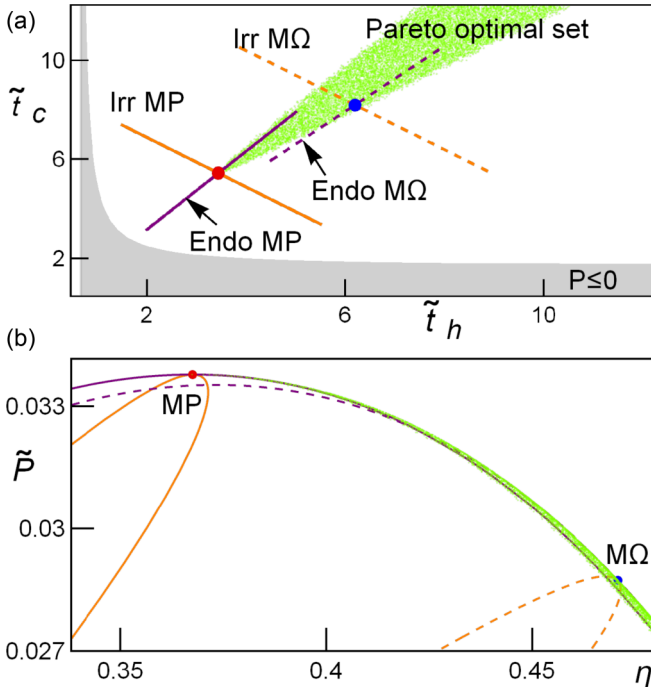


FIG. 6. In (a) the optimal set and in (b) the Pareto front. Endoreversible or irreversible limits are depicted as well (purple and orange), in dashed. Here  $\tau = 2/5$  and  $\Sigma = 1$  as a representative case.

where  $A$  and  $B$  are positive constants, giving the restitution strength.<sup>1</sup>

In a linear approximation the local stability of this steady state is determined by the eigenvalues,  $\lambda_1$  and  $\lambda_2$ , and eigenvectors of the Jacobian matrix:

$$\mathcal{J} = - \begin{bmatrix} A \frac{\partial \tilde{Q}_c}{\partial t_c} \Big|_{\tilde{t}_c^*, \tilde{t}_h^*} & 0 \\ 0 & B \frac{\partial \tilde{Q}_h}{\partial t_h} \Big|_{\tilde{t}_c^*, \tilde{t}_h^*} \end{bmatrix}.$$

Relaxation times,  $t_1 \equiv \lambda_1^{-1}$  and  $t_2 \equiv \lambda_2^{-1}$  are [50]

$$t_i^{\text{MP}} = \frac{4}{\eta_C^2 I_i} [\sqrt{\Sigma(1 - \eta_C)} + 1]^2, \quad (50)$$

$$t_i^{\text{M}\Omega} = \frac{4}{\eta_C^2 I_i} \left[ \frac{\sqrt{2\Sigma(1 - \eta_C)}}{2 - \eta_C} + 1 \right]^2 (2 - \eta_C), \quad (51)$$

where  $i = \{1, 2\}$ ,  $I_1 = A$ , and  $I_2 = B$ . The operation and relaxation times are proportional,

$$t_{\text{relax}}^* \equiv t_1^* + t_2^* = 2 \left( \frac{A^{-1} + B^{-1}}{\eta_C} \right) \tilde{t}_{\text{tot}}^* = \frac{2z}{\eta_C} \tilde{t}_{\text{tot}}^*, \quad (52)$$

where  $z \equiv A^{-1} + B^{-1}$  is the same for both regimes. In a cyclic process the system should remain close to the steady state within a cycle time, thus  $t_{\text{relax}}^* \leq \tilde{t}_{\text{tot}}^*$ , constraining  $A$  and  $B$

<sup>1</sup>An alternative interpretation is to associate stability to “forces” stemming by the well-known harmonic oscillator potential [ $V_x = V_x(\tilde{t}_x)$ ], fulfilling that  $d\tilde{t}_x/dt = -dV_x/d\tilde{t}_x$ , each one with a minimum located at  $\tilde{t}_x^*$ , where  $V_x = 0$ . In this way,  $d\tilde{t}_x/dt = -dV_x/d\tilde{t}_x = -d^2V_x/d\tilde{t}_x^2|_{\tilde{t}_x^*}(\tilde{t}_x - \tilde{t}_x^*)$  with  $d^2V_x/d\tilde{t}_x^2|_{\tilde{t}_x^*} \geq 0$ .

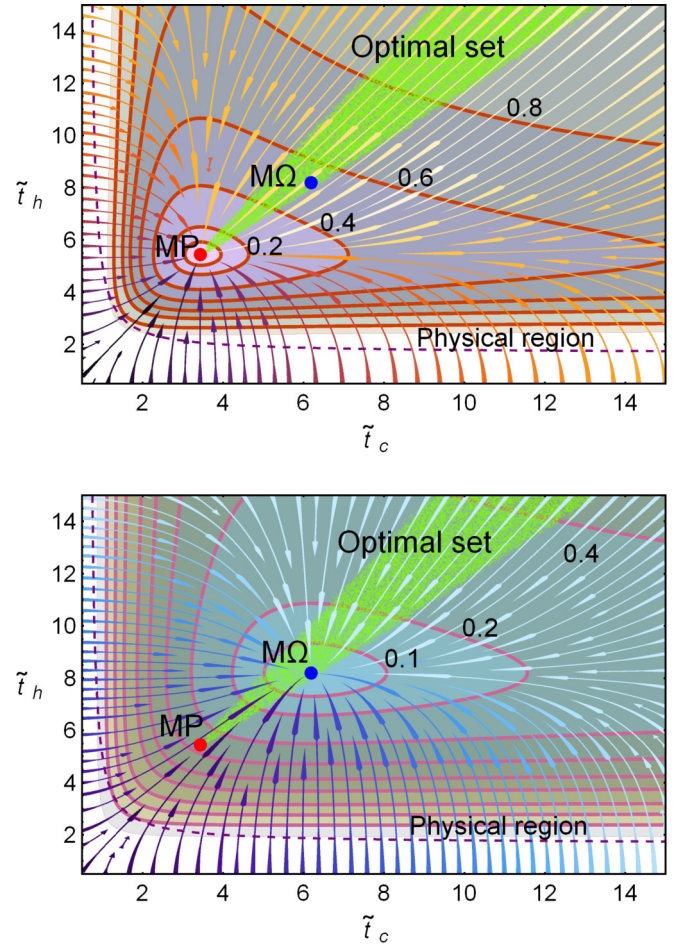


FIG. 7. Stream plots of the dynamics given by Eqs. (48) and (49) for the case where  $t_{\text{relax}}^{\text{MP}} = \tilde{t}_{\text{tot}}^{\text{MP}}$  for the MP regime in (a) and  $t_{\text{relax}}^{\text{M}\Omega} = \tilde{t}_{\text{tot}}^{\text{M}\Omega}$  for MΩ in (b). Level curves of constant velocities,  $v_{\text{dyn}}$  [see Eq. (54)], are displayed to show patterns over time and how fast the velocity changes as the systems head toward the steady state.  $\tau = 2/5$  and  $\Sigma = 1$  are used.

(determining the restitution strength)

$$z \leq \frac{\eta_C}{2}. \quad (53)$$

Beyond the linear approximation, the system given by Eqs. (48) and (49) can be solved numerically. In Fig. 7 it is shown the stream plot of the complete dynamics, showing the existence of a stable point. Level curves for the dynamical velocity  $v_{\text{dyn}}$  are depicted,

$$v_{\text{dyn}} = \sqrt{(d\tilde{t}_c/dt)^2 + (d\tilde{t}_h/dt)^2} = \text{const} \quad (54)$$

to show the patterns over time and how fast the velocity changes as the systems head toward the steady state. For the MP case these contours are closer to the steady state and depict a faster transition to the stable point than in the MΩ case, shown in Fig. 7(b).

In both regimes faster transitions occur when  $\tilde{t}_c < \tilde{t}_c^*$  and  $\tilde{t}_h < \tilde{t}_h^*$ . Near the stable point velocities are slightly slower in the  $t_c$  direction but as the perturbations increase the  $\tilde{t}_c$  axis becomes much slower, pushing the system further away. A more symmetric situation is obtained in the MΩ case.

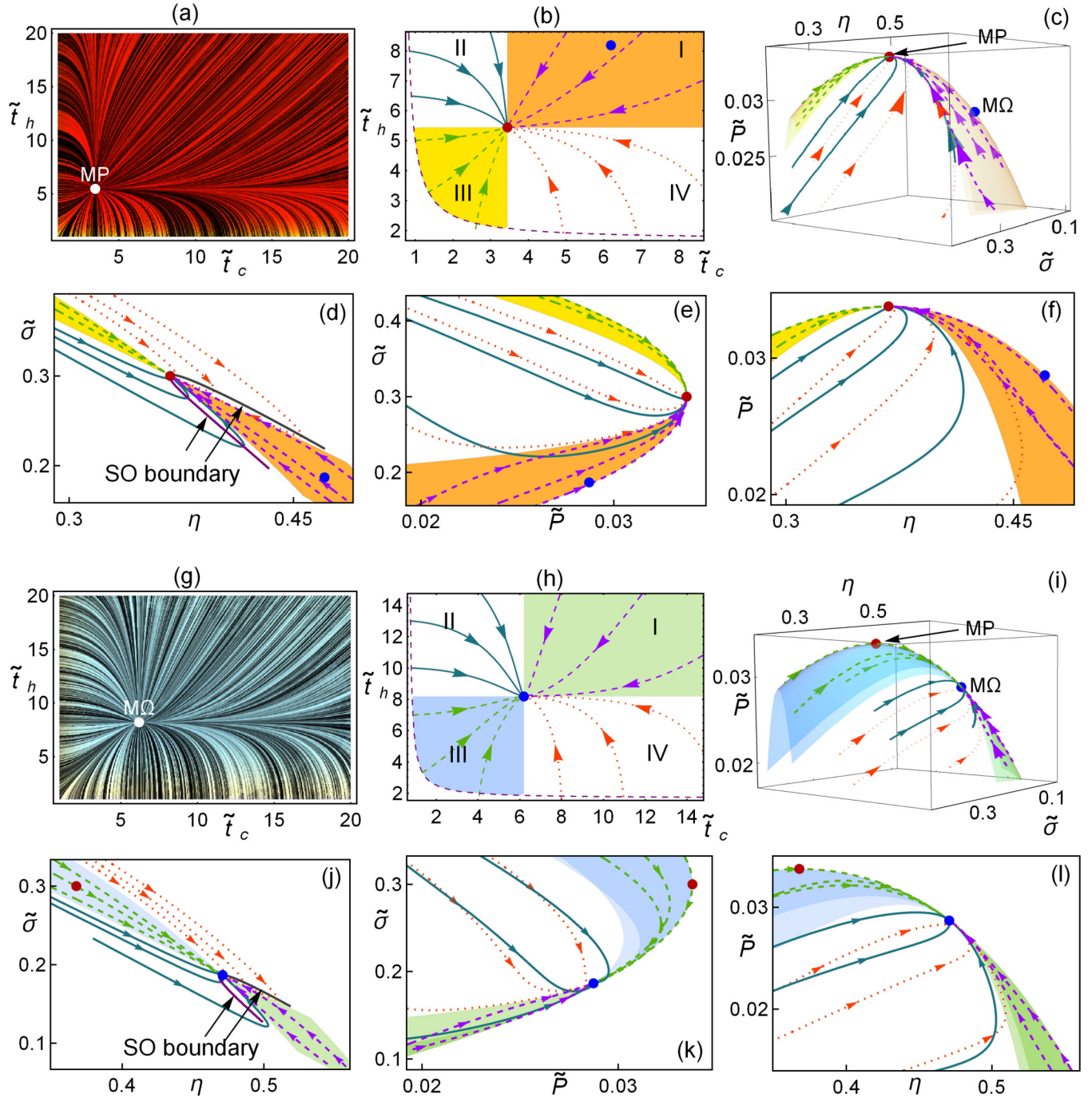


FIG. 8. Stability around the operation regimes. In (a) and (g) the line integral convolution plot of Eqs. (48) and (49), which simulate stream lines of fixed arc length over a set of random initial conditions (denoted by transitions from yellow  $\rightarrow$  red  $\rightarrow$  black). [(b) and (h)] Trajectories for the solution of the system Eqs. (48) and (49) in the phase space. (c) Trajectories toward relaxation in the  $\eta$ - $\tilde{P}$ - $\tilde{\sigma}$  surface corresponding to all possible  $\tilde{t}_c$  and  $\tilde{t}_h$  values. [(d)–(f) and (j)–(l)] Trajectories in the efficiency vs entropy production plane, power output vs entropy production plane and efficiency vs power plane, respectively. In all cases  $\Sigma = 1$ ,  $\tau = 2/5$  and  $A$  and  $B$  are chosen to fulfill that  $A = B$  and  $t_{\text{relax}}^{\text{MP}} = \tilde{t}_{\text{tot}}^{\text{MP}}$  as a representative case, the qualitative behavior for other parameters is equivalent. The stability-induced optimization (SO) boundary region is depicted in (d) and (j).

Figure 8 displays some behaviors linked to the stability around the MP state. Figure 8(a) shows the line integral convolution plot of Eqs. (48) and (49) over a random distribution of initial conditions, simulating stream lines. Figure 8(b) shows representative relaxation trajectories. Regions I–IV indicate where  $\tilde{t}_c$  and  $\tilde{t}_h$  are larger or smaller than  $\tilde{t}_c^{\text{MP}}$  and  $\tilde{t}_h^{\text{MP}}$ ,

respectively. They are shaded in different colors to emphasize differences among these trajectories in the different energetic planes plotted in Figs. 8(c)–8(f). Notice that trajectories in each quadrant evolve in a slightly different way, which yields to noticeable energetic repercussions. Of special relevance are regions I and III, colored in orange and yellow, respectively.

In Fig. 8(c) the  $\tilde{\sigma}$ - $\eta$ - $\tilde{P}$  surface describes a sharp crest whose lateral sides are associated to states in regions II and IV; meanwhile, the shoulders are associated to regions I and III. Figures 8(d)–8(f) show that regions I and III have straight relaxation trajectories to the stable point and the best compromise between power and efficiency. The trajectories in region I, contrary to those of region III, have the lesser entropy production and evolves a decreasing efficiency at the time that entropy increases.

In regions II and IV there are wider areas in which trajectories decrease entropy production, increasing efficiency and power output. In this sense, region III and most of II and IV are linked to trajectories in which the engine experiences an optimization induced by stability, coincidentally, located where transitions to the stable point are faster (see Fig. 7).

When the contours start to separate, the velocity in the relaxation starts to increase. According to Fig. 8 there is some point at which relaxation paths exhibit a decreasing efficiency and increasing entropy production [see Fig. 8(d)]. By looking at the derivatives of the contours of constant velocities, it is possible to define a region linking how fast the system evolves and where simultaneous optimization occurs. This is done by means of the derivative of Eq. (54) ( $dv_{\text{dyn}}/dt$ , see Fig. 7) and constraining the resulting slope to a certain value. This will be referred as a region of self-optimization. The boundary of this region is explicitly depicted in Fig. 8(d).

It is noteworthy that the region of no-self-optimization coincides with the region where the system takes longer to arrive to the stable state (see Fig. 7). This means that self-optimization while arriving to the steady state is achieved fast, meanwhile in the no self-optimization the evolution is slowly, but these trajectories spend more time in the region toward the Pareto front. This feature will have repercussions in the statistical behavior of many perturbations as will be discussed later.

The consequences of the dynamics on the system energetic properties could imply the use of a disadvantage, such as limited control, to yield a favorable self-optimization mechanism. For this purpose one could search, for instance, a biased control to favor perturbations in some region of the phase space.

In order to get insights about these issues, the influence of continuous random perturbations over a cycle is addressed below.

### C. Random perturbations and Markovian cycle to cycle performance

The  $N$  steps are computed by solving the stochastic differential equation based on Eqs. (48) and (49), using normally distributed random variables following a two-dimensional Gaussian distribution,  $\{\xi_1, \xi_2\}$  in the  $\{\tilde{t}_c, \tilde{t}_h\}$  directions, as additive white noise and using the Euler-Maruyama method,

$$\Delta\tilde{t}_c = A[\tilde{Q}_c(\tilde{t}_c^*, \tilde{t}_h^*) - \tilde{Q}_c(\tilde{t}_c, \tilde{t}_h)]\Delta t + \xi_1\sqrt{\Delta t}, \quad (55)$$

$$\Delta\tilde{t}_h = B[\tilde{Q}_h(\tilde{t}_c^*, \tilde{t}_h^*) - \tilde{Q}_h(\tilde{t}_c, \tilde{t}_h)]\Delta t + \xi_2\sqrt{\Delta t}, \quad (56)$$

where  $\xi_1$  and  $\xi_2$  follow the Gaussian distribution,

$$f_{\xi}(\tilde{t}_c, \tilde{t}_h) = \frac{\beta^2}{2\pi\tilde{t}_c^*\tilde{t}_h^*} e^{-\frac{\beta^2}{2}[(\frac{\tilde{t}_c}{\tilde{t}_c^*})^2 + (\frac{\tilde{t}_h}{\tilde{t}_h^*})^2]}, \quad (57)$$

and  $\beta$  is such that standard deviation  $\sigma_{\tilde{t}_c} = \tilde{t}_c^*/\beta$  and  $\sigma_{\tilde{t}_h} = \tilde{t}_h^*/\beta$ . The initial state is  $(\tilde{t}_{c1}, \tilde{t}_{h1}) = (\tilde{t}_c^*, \tilde{t}_h^*)$ ;  $\Delta t$  is  $\tilde{t}_{\text{tot}}^*/10^4$ , so that after  $10^4$  steps one cycle is fulfilled.  $A = B = 40/\eta_C$ , stemming from requiring that  $t_{\text{relax}} = \tilde{t}_{\text{tot}}^*/10$  [see Eq. (53) from the linear approximation].

After one cycle has ended, the system starts another random trajectory starting from the steady state, without any information regarding previous cycles. This procedure is repeated for  $5 \times 10^4$  trajectories or cycles. The statistical convergence is tested using the Kullback-Leibler divergence of the system energetic distributions (see Appendix). The results are shown in Fig. 9. In Fig. 9(a) the averaged states for each trajectory are depicted making a distinction on whether in average the system is inside the stability-induced optimization region or not. Despite of covering a significantly smaller area, green points comprise 47% of the trajectories. In most of the blue region the system converges faster to the steady state, and, thus, it is more likely that the system is closer to it than in the green region where transitions are slower. The faster decay corresponds to an overall improvement, the slower type of trajectories keep the system in a less entropy and larger efficiency state for longer. The result is an average performance improvement. To notice this displacement in the averaged states, the distinction according to quadrants (I–IV, see Fig. 8) is depicted in Fig. 9(b). In both figures the geometric centers of the depicted points in each region are displaced toward the direction at which the optimal set is found.

In Fig. 9(c) the fluctuations of  $\eta$  vs  $\tilde{\sigma}$  around the steady state are depicted, these fluctuations are given by

$$\text{Fluc}(\eta) = (\eta^{\text{MP}} - \langle \eta \rangle)^2, \quad (58)$$

$$\text{Fluc}(\tilde{\sigma}) = (\tilde{\sigma}^{\text{MP}} - \langle \tilde{\sigma} \rangle)^2, \quad (59)$$

where  $\langle \rangle$  refers to average over one trajectory. In the green region these fluctuations form a sharper region (less dispersion). In Fig. 9(d) the  $\tilde{\eta}$  vs  $\tilde{P}$  plane is analyzed. Again, the endoreversible limit is an upper bound of the thermodynamic performance of many trajectories. Those cases of improving  $\eta$ ,  $\tilde{\sigma}$ , and  $\tilde{P}$  are located around the irreversible limit. Green points reproduce a compromise in which power is sacrificed in order to increase efficiency and diminish entropy production. Additionally, less fluctuations comes with smaller drops in power.

## V. CONCLUDING REMARKS AND PERSPECTIVES

The local stability of the maximum power and maximum Omega regimes have been analyzed under two different dynamics. One with perturbations on the output heat flux and the power output and another one with perturbations on the input or output heats.

Relaxation trajectories are such that far from the steady state they exhibit a simultaneous improvement of power, efficiency, and entropy production with trajectories that approach

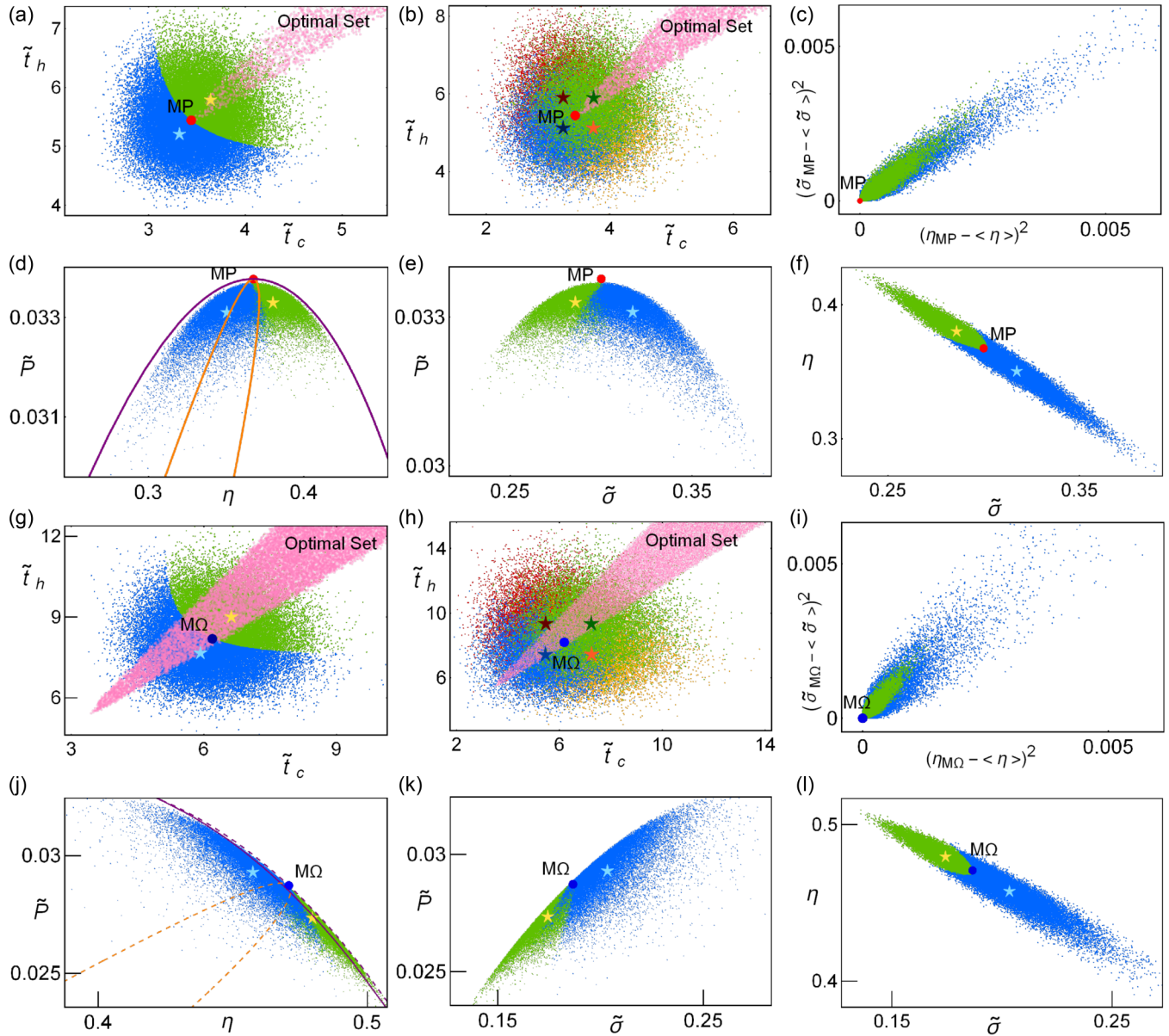


FIG. 9. In (a) the averaged position in each cycle or trajectory is shown. Colors indicate whether trajectories starting at the average state would exhibit a simultaneous improvement of  $\eta$ ,  $\tilde{P}$ , and  $\tilde{\sigma}$  (blue points) or the increasing of power comes hand in hand with decreasing efficiency and increasing entropy production (green points). In a close caption the average displacement of each type of points (light blue and yellow stars) and the overall performance (red cross) is depicted. The latter is slightly moved onto the direction of the optimal set. In (b) the final points after each trajectory are shown but having under consideration in which quadrant the trajectory remains in average. These final points have the same behavior as the average states but are more spread out. A close-caption shows that the averages in each quadrant (stars with colors according to Fig. 8) are displaced toward quadrant I. In (c) the fluctuations in efficiency vs fluctuations in entropy production, green trajectories are much less spread, mean values for green and blue points are denoted by light blue and yellow stars. In (d) the results of  $\eta$  vs  $\tilde{P}$  are shown. In (e) and (f) the behavior of power output and efficiency according to the entropy generation are shown. In both cases green points are closer to the steady state, according to the means indicated by stars. For this case  $A = B = 4/(1 - \tau)$  so that  $t_{\text{relax}}^{\text{MP}} = \tilde{t}_{\text{tot}}^{\text{MP}}$ ,  $\Delta t$  is  $\tilde{t}_{\text{tot}}^{\text{MP}}/10^4$ ,  $\sigma_\alpha = \alpha^{\text{MP}}/10$ ,  $\sigma_\tau = \tilde{t}^{\text{MP}}/10$ ,  $\tau = 2/5$  and  $\Sigma = 1$ , this is a representative case, but the behavior for other combinations of parameters is the same. In (g)–(l) the same is done for the  $M\Omega$  regime.

to the Pareto front, which gives the best compromise among the most relevant thermodynamic quantities of the system, in a multiobjective optimization perspective. It is shown that the Pareto front is an upper envelop of the endoreversible limit (resulting from constraining the partial contact times with the external thermal baths).

An analysis of consecutive random perturbations has been addressed. Trends due to the proposed dynamics appear in the statistical behavior of many cycles, indicating a link between the overall behavior and the Pareto front. The accuracy of the statistical treatment is supported by the Kullback-Leibler divergence approaching zero, thus, adding more

trajectories makes no difference in the statistical description of the problem.

In the first dynamics there is a basin of attraction and a nullcline linked to the restitution forces involved in the dynamics. Outside the attraction basin, relaxation trajectories lead the system to a nonphysical region. The endoreversible limit is an attractor in the relaxation far from the steady state. Meanwhile near the steady state the so-called irreversible limit, stemming from fixing the operation time, plays a role in determining which trajectories arrive to the steady state. For many stochastic trajectories the nullcline has a relevant influence on the final points of each trajectory [see Fig. 4(a)]. By separating points having a final state inside or outside the attraction basin different energetic behaviors are obtained with energetic Gaussian distributions displaced from the steady state in opposite directions. Inside the stability basin there is a decreasing efficiency and increasing entropy production while the contrary occurs for points outside. Averaged energetic states and final states are compared, showing that the endoreversible limit is an energetic upper boundary and the irreversible behavior is an attractor of both: final and averaged states in each trajectory.

The second dynamics always exhibits a stable state revealing a relation between how fast the system arrives to it and whether the trajectory describes a simultaneous optimization of power output, efficiency, and entropy production. Fast transitions occur where the system exhibits a simultaneous improvement of efficiency and entropy production. In the no self-optimization region transitions are slow but the system remains over the Pareto front for longer periods. In the analysis of many stochastic trajectories the irreversible limit acts an attractor for trajectories that experience either simultaneous improvement or a simultaneous increment of entropy production and decrements of efficiency (fast or slow relaxations, respectively). Thus, under persistent perturbations the net effect is to drive the system toward the Pareto front.

In both dynamics the relaxation time is of the order of the operation time or less to guarantee cyclic processes. For completeness, combinations of the size of the perturbations and restitution strengths (given by  $A$ ,  $B$ ,  $C$ , and  $D$ ) have been tested and the obtained behaviors are found to be qualitatively similar. One thing to notice in the 1st dynamics is that quite strong restitution forces might act against the system stability, its effect being equivalent to consecutive perturbations during an enough extended period of time. This can be seen from Eqs. (31) and (32), where increments in  $C$  and  $D$  can be compensated by shorter steps in the stochastic trajectories and a larger stochastic variable, or equivalently, to having larger steps  $\Delta t$  (larger dynamical time) but smaller influence of the stochastic variable.

The above results indicate that for weakly dissipative heat engines there could be an optimization induced by stability, either under a sole perturbation or due to consecutive stochastic noise. In this sense, a limited control in the operation variables or biased control might turn out in favor of the system performance. Some examples in which this analysis could be of interest are (i) a low-dissipation micrometric HE experimentally realized by a single particle in an optical trap through an optical harmonic potential [73,74]; (ii) a spin vortex confined on a disk with a harmonic potential [75,76];

and (iii) a macroscopic solarized irreversible Brayton engine with fluctuations in the operation variables. In all these cases their stability dynamics could be addressed in an equivalent way but eventually depending on the natural variables of each model.

For the first system it has been established that it can be described by the low-dissipation model. For the second example the modeling of the system by means of the low-dissipation model represents an ongoing task that needs to be confirmed, although the dynamic is the analog to that of the optical trap with a confining potential that corresponds to the one addressed in this paper. The representation of the Brayton and Otto systems in terms of the low-dissipation model needs further research as well. In previous works the Otto and Brayton cycles have been related with the irreversible Carnot cycle [13], where the linking of both models depends on the heat capacity of the working fluid. Furthermore, the irreversible Carnot model has been linked to the low-dissipation model, where the mapping between these two models is constrained to a certain family of heat capacities [70]. Thus, it is expected that the Otto and Brayton heat engines can be mapped into the low-dissipation model. For a nonregenerative irreversible Brayton cycle this can be done by matching entropy changes in both models, obtaining:

$$\Sigma_h/t_h = m C_V \ln \left[ r_p^{-\frac{1-\gamma}{\gamma}} + \eta_c^{-1} (1 - r_p^{-\frac{1-\gamma}{\gamma}}) \right], \quad (60)$$

$$\Sigma_c/t_c = m C_V \ln \left[ r_p^{\frac{1-\gamma}{\gamma}} - \eta_t (r_p^{\frac{1-\gamma}{\gamma}} - 1) \right], \quad (61)$$

where  $m$  is the working fluid mass,  $C_V$  is the heat capacity at constant volume,  $\gamma \equiv C_p/C_V$  is the adiabatic factor,  $r_p$  is the pressure ratio, and  $(\eta_c, \eta_t)$  are the isentropic efficiencies of the compressor and turbine, respectively. External perturbations on this device arise, for instance, if the turbine is combined with a solar collector and fluctuations in the direct solar irradiance due to meteorological conditions (cloudy days induce a power law distribution). A completely analog description of the Otto engine can be done, where external perturbations could arise from cycle-to-cycle combustion variability.

In the line of thought of a unified study of HE's and RE's [58], it is expected that the extension of the analysis here reported could yield to similar results for refrigerator devices, which is still a work in progress.

A possible perspective on this subject is the study of lack of control in more specific systems to get hints on natural optimization requirements, or "natural optimization preferences" [85–90]. Let us recall that the nondominance concept used to obtain the Pareto front uses the same weight in all the objective functions, then, inference of a hierarchy in the objective functions could shed some light regarding evolutionary adaptation in specialized systems [91].

#### ACKNOWLEDGMENTS

Authors acknowledge financial support from Universidad de Salamanca Contract No. 2017/X005/1, Junta de Castilla y León Project No. SA017P17, and National Natural Science Foundation of China (Grant No. 11405032).

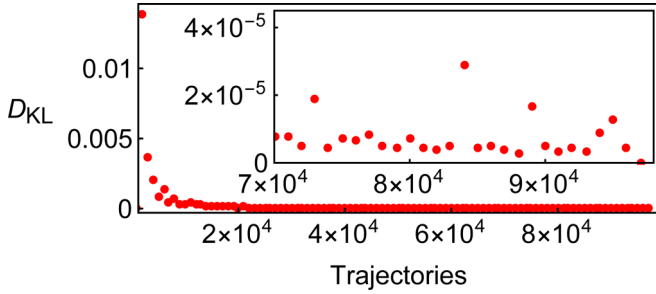


FIG. 10. Kullback-Leibler divergence comparison at every 1000 trajectories or cycles. A good convergence is obtained for the number of trajectories analyzed in Sec. III E.

**APPENDIX: NUMBER OF TRAJECTORIES FOR STATISTICAL CONVERGENCE**

**1. Dynamics involving  $\tilde{Q}_c$  and  $\tilde{P}$**

Before, it was mentioned the use of the Kullback-Leibler divergence,  $D_{KL}$  [81], to test statistical convergence.  $D_{KL}$  gives a measure of how distant are two distributions, so that if its value is zero, then the information stemming from both distributions is the same. Since this is a relevant issue to demonstrate that the obtained trend is not due to the lack of additional data, the details of the divergence are addressed here.

For this test the evolution in the discrete probability distribution for the power will be used. From the averaged  $\tilde{P}$  in  $N \geq 1000$  trajectories, the interval between the largest and smallest  $\tilde{P}$  value is divided in  $\sqrt{N}$  (rounded to the upper next integer) equal intervals or bins of length  $\Delta\tilde{P}$ . From this partition the discrete probability distribution of the first  $2k$ -thousand trajectories,  $\rho_k$  are obtained. The Kullback-Leibler divergence is calculated comparing  $\rho_{k-1}$  with  $\rho_k$ ,  $D_{KL,k}$  according to Eq. (A1).

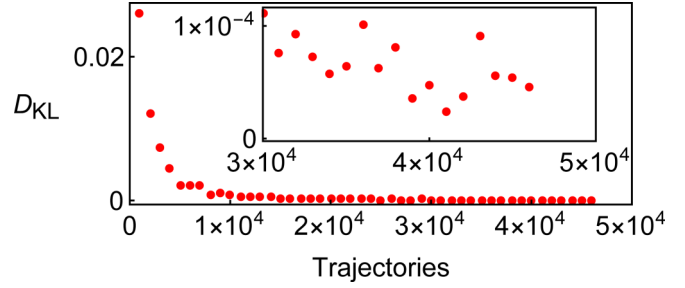


FIG. 11. Kullback-Leibler divergence comparison at every 1000 trajectories or cycles. A good convergence is obtained for the number of trajectories analyzed in Sec. IV C.

The resulting  $D_{KL,k}$  values are shown in Fig. 10 for  $N = 10^5$  trajectories, showing that from  $7 \times 10^4$  trajectories the statistical behavior does not vary significantly and adding more trajectories will not give much further information.

**2. Dynamics involving  $\tilde{Q}_c$  and  $\tilde{Q}_h$**

From the averaged  $\tilde{P}$  values computed of  $N \geq 1000$  trajectories, the interval between the largest and smallest  $\tilde{P}$  values is divided by  $\sqrt{N}$  (rounded to the upper next integer) equal intervals, or bins, in this way, the same partition is used for the to compute the discrete probability distributions of the first  $k$ -thousand trajectories,  $\rho_k$  are obtained, and the  $D_{KL}$  is calculated comparing  $\rho_{k-1}$  with  $\rho_k$ .  $D_{KL,k}$  is given by

$$D_{KL,k}(\rho_{k-1} \parallel \rho_k) = - \sum_i \rho_{k-1,i} \log \left( \frac{\rho_{k,i}}{\rho_{k-1,i}} \right), \quad (A1)$$

giving a measure of how much information is gained by adding more trajectories. In Fig. 11, it is shown that from  $4 \times 10^4$  trajectories the statistical behavior does not vary significantly and adding trajectories will not provide much further information.

[1] M. O. Scully, M. S. Zubairy, G. S. Agarwal, and H. Walther, Extracting work from a single heat bath via vanishing quantum coherence, *Science* **299**, 862 (2003).

[2] R. Dillenschneider and E. Lutz, Energetics of quantum correlations, *Europhys. Lett.* **88**, 50003 (2009).

[3] G. Benenti, K. Saito, and G. Casati, Thermodynamic Bounds on Efficiency for Systems with Broken Time-Reversal Symmetry, *Phys. Rev. Lett.* **106**, 230602 (2011).

[4] X. L. Huang, T. Wang, and X. X. Yi, Effects of reservoir squeezing on quantum systems and work extraction, *Phys. Rev. E* **86**, 051105 (2012).

[5] O. Abah and E. Lutz, Efficiency of heat engines coupled to nonequilibrium reservoirs, *Europhys. Lett.* **106**, 20001 (2014).

[6] J. Roßnagel, O. Abah, F. Schmidt-Kaler, K. Singer, and E. Lutz, Nanoscale Heat Engine Beyond the Carnot Limit, *Phys. Rev. Lett.* **112**, 030602 (2014).

[7] M. Polettni, G. Verley, and M. Esposito, Efficiency Statistics at all Times: Carnot limit at Finite Power, *Phys. Rev. Lett.* **114**, 050601 (2015).

[8] W. Niedenzu, D. Gelbwaser-Klimovsky, A. G. Kofman, and G. Kurizki, On the operation of machines powered by quantum non-thermal baths, *New. J. Phys.* **18**, 083012 (2016).

[9] G. Manzano, F. Galve, R. Zambrini, and J. M. R. Parrondo, Entropy production and thermodynamic power of the squeezed thermal reservoir, *Phys. Rev. E* **93**, 052120 (2016).

[10] J. Klaers, S. Faelt, A. Imamoglu, and E. Togan, Squeezed thermal Reservoirs as a Resource for a Nanomechanical Engine Beyond the Carnot Limit, *Phys. Rev. X* **7**, 031044 (2017).

[11] J. S. Lee and H. Park, Carnot efficiency is reachable in an irreversible process, *Sci. Rep.* **7**, 10725 (2017).

[12] W. Niedenzu, V. Mukherjee, A. Ghosh, A. G. Kofman, and G. Kurizki, Quantum engine efficiency bound beyond the second law of thermodynamics, *Nat. Commun.* **9**, 165 (2018).

[13] J. Gonzalez-Ayala, L. A. Arias-Hernandez, and F. Angulo-Brown, Connection between maximum-work and maximum-power thermal cycles, *Phys. Rev. E* **88**, 052142 (2013).

[14] F. L. Curzon and B. Ahlborn, Efficiency of a Carnot engine at maximum power output, *Am. J. Phys.* **43**, 22 (1975).

[15] T. Schmiedl and U. Seifert, Efficiency of molecular motors at maximum power, *Europhys. Lett.* **83**, 30005 (2008).



- [16] C. Van den Broeck, N. Kumar, and K. Lindenberg, Efficiency of Isothermal Molecular Machines at Maximum Power, *Phys. Rev. Lett.* **108**, 210602 (2012).
- [17] N. Golubeva and A. Imparato, Efficiency at Maximum Power of Interacting Molecular Machines, *Phys. Rev. Lett.* **109**, 190602 (2012); *Phys. Rev. Lett.* **110**, 149902(E) (2013).
- [18] Y. Apertet, H. Ouerdane, C. Goupil, and P. Lecoeur, Efficiency at maximum power of thermally coupled heat engines, *Phys. Rev. E* **85**, 041144 (2012).
- [19] R. Wang, J. Wang, J. He, and Y. Ma, Efficiency at maximum power of a heat engine working with a two-level atomic system, *Phys. Rev. E* **87**, 042119 (2013).
- [20] F. Wu, J. He, Y. Ma, and J. Wang, Efficiency at maximum power of a quantum Otto engine: Both within finite-time and irreversible thermodynamics, *Phys. Rev. E* **90**, 062134 (1990).
- [21] Y. Izumida, K. Okuda, J. M. M. Roco, and A. Calvo Hernández, Heat devices in nonlinear irreversible thermodynamics, *Phys. Rev. E* **91**, 052140 (2015).
- [22] S. Q. Sheng and Z. C. Tu, Hidden symmetries and nonlinear constitutive relations for tight-coupling heat engines, *New J. Phys.* **17**, 045013 (2015).
- [23] Y. Izumida and K. Okuda, Linear irreversible heat engines based on the local equilibrium assumptions, *New J. Phys.* **17**, 085011 (2015).
- [24] H. Ouerdane, Y. Apertet, C. Goupil, and P. Lecoeur, Continuity and boundary conditions in thermodynamics: From Carnot's efficiency to efficiencies at maximum power, *Eur. Phys. J. Spec. Top.* **224**, 839 (2015).
- [25] F. Angulo-Brown, An ecological optimization criterion for finite-time heat engines, *J. Appl. Phys.* **69**, 7465 (1991).
- [26] A. Calvo Hernández, A. Medina, J. M. M. Roco, J. A. White, and S. Velasco, Unified optimization criterion for energy converters, *Phys. Rev. E* **63**, 037102 (2001).
- [27] J. W. Stucki, The optimal efficiency and the economic degrees of coupling of oxidative phosphorylation, *Eur. J. Biochem.* **109**, 269 (1980).
- [28] R. Long and W. Liu, Unified trade-off optimization for general heat devices with nonisothermal processes, *Phys. Rev. E* **91**, 042127 (2015).
- [29] R. Long and W. Liu, Ecological optimization for general heat engines, *Physica A* **434**, 232 (2015).
- [30] V. Singh and R. S. Johal, Feynman's ratchet and pawl with ecological criterion: Optimal performance versus estimation with prior information, *Entropy* **19**, 576 (2017).
- [31] I. Iyyappan and M. Ponnuragan, Thermoelectric energy converters under a trade-off figure of merit with broken time-reversal symmetry, *J. Stat. Mech.* (2017) 093207.
- [32] C. Lu and L. Bai, Nonlinear dissipation heat devices in finite-time thermodynamics: An analysis of the trade-off optimization, *J. Non-Equilib. Thermodyn.* **42**, 277 (2017).
- [33] M. Esposito, K. Lindenberg, and C. Van den Broeck, Universality of Efficiency at Maximum Power, *Phys. Rev. Lett.* **102**, 130602 (2009).
- [34] J. Guo, J. Wang, Y. Wang, and J. Chen, Universal efficiency bounds of weak-dissipative thermodynamic cycles at the maximum power output, *Phys. Rev. E* **87**, 012133 (2013).
- [35] Y. Zhang, C. Huang, G. Lin, and J. Chen, Universality of efficiency at unified trade-off optimization, *Phys. Rev. E* **93**, 032152 (2015).
- [36] R. Uzdin and R. Kosloff, Universal features in the efficiency at maximum work of hot quantum Otto engines, *Europhys. Lett.* **108**, 40001 (2014).
- [37] S. Q. Sheng and Z. C. Tu, Constitutive relation for nonlinear response and universality of efficiency at maximum power for tight-coupling heat engines, *Phys. Rev. E* **91**, 022136 (2015).
- [38] B. Cleuren, B. Rutten, and C. Van den Broeck, Universality of efficiency at maximum power: Macroscopic manifestation of microscopic constraints, *Eur. Phys. J. Spec. Top.* **224**, 879 (2015).
- [39] V. Holubec and A. Ryabov, Maximum efficiency of low-dissipation heat engines at arbitrary power, *J. Stat. Mech.* (2016) 073204.
- [40] N. Shiraishi, K. Saito, and H. Tasaki, Universal Trade-Off Relation Between Power and Efficiency for Heat Engines, *Phys. Rev. Lett.* **117**, 190601 (2016).
- [41] Z. Ye, Y. Hu, J. He, and J. Wang, Universality of maximum-work efficiency of a cyclic heat engine based on a finite system of ultracold atoms, *Sci. Rep.* **7**, 6289 (2017).
- [42] I. Iyyappan and M. Ponnuragan, General relations between the power, efficiency, and dissipation for the irreversible heat engines in the nonlinear response regime, *Phys. Rev. E* **97**, 012141 (2018).
- [43] M. Bauer, K. Brandner, and U. Seifert, Optimal performance of periodically driven, stochastic heat engines under limited control, *Phys. Rev. E* **93**, 042112 (2016).
- [44] P. Pietzonka and U. Seifert, Universal Trade-Off Between Power, Efficiency, and Constancy in Steady-State Heat Engines, *Phys. Rev. Lett.* **120**, 190602 (2018).
- [45] V. Holubec and A. Ryabov, Cycling Tames Power Fluctuations Near Optimum Efficiency, *Phys. Rev. Lett.* **121**, 120601 (2018).
- [46] K. Proesmans, Y. Dreher, M. Gavrilov, J. Bechhoefer, and C. Van den Broeck, Brownian Duet: A Novel Tale of Thermodynamic Efficiency, *Phys. Rev. X* **6**, 041010 (2016).
- [47] K. Funo and M. Ueda, Work Fluctuation-Dissipation Trade-Off in Heat Engines, *Phys. Rev. Lett.* **115**, 260601 (2015).
- [48] R. Uzdin, A. Levy, and R. Kosloff, Equivalence of Quantum Heat Machines, and Quantum-Thermodynamic Signatures, *Phys. Rev. X* **5**, 031044 (2015).
- [49] R. Kosloff and Y. Rezek, The quantum harmonic Otto cycle, *Entropy* **19**, 136 (2017).
- [50] I. Reyes-Ramírez, J. Gonzalez-Ayala, A. Calvo Hernández, and M. Santillán, Local-stability analysis of a low-dissipation heat engine working at maximum power output, *Phys. Rev. E* **96**, 042128 (2017).
- [51] J. Gonzalez-Ayala, M. Santillán, I. Reyes-Ramírez, and A. Calvo Hernández, Link between optimization and local stability of a low dissipation heat engine: Dynamic and energetic behaviors, *Phys. Rev. E* **98**, 032142 (2018).
- [52] J. Gonzalez-Ayala, M. Santillán, M. J. Santos, A. Calvo Hernández, and J. M. M. Roco, Optimization and stability of heat engines: The role of entropy evolution, *Entropy* **20**, 865 (2018).
- [53] D. Bercioux, R. Egger, P. Hänggi, and M. Thorwart, Focus on nonequilibrium fluctuation relations: From classical to quantum, *New J. Phys.* **17**, 020201 (2015).
- [54] J. M. Horowitz and K. Jacobs, Energy Cost of Controlling Mesoscopic Quantum Systems, *Phys. Rev. Lett.* **115**, 130501 (2015).

- [55] B. B. Machta, Dissipation Bound for Thermodynamic Control, *Phys. Rev. Lett.* **115**, 260603 (2015).
- [56] A. C. Barato and U. Seifert, Thermodynamic cost of external control, *New J. Phys.* **19**, 073021 (2017).
- [57] M. Esposito, R. Kawai, K. Lindenberg, and C. Van den Broeck, Efficiency at Maximum Power of Low-Dissipation Carnot Engines, *Phys. Rev. Lett.* **105**, 150603 (2010).
- [58] J. Gonzalez-Ayala, A. Medina, J. M. M. Roco, and A. Calvo Hernández, Irreversible and endoreversible behaviors of the low-dissipation-model for heat devices: The role of the time constraints and symmetries on the performance at maximum  $\chi$  figure of merit, *J. Stat. Mech.* (2016) 073202.
- [59] J. Guo, J. Wang, Y. Wang, and J. Chen, Efficiency of two-level weak dissipation quantum Carnot engines at the maximum power, *J. Appl. Phys.* **113**, 143510 (2013).
- [60] A. Calvo Hernández, A. Medina, J. M. M. Roco, Time, entropy generation, and optimization in low-dissipation heat devices, *New J. Phys.* **17**, 075011 (2015).
- [61] V. Holubec and R. Artem, Efficiency at and near maximum power of low-dissipation heat engines, *Phys. Rev. E* **92**, 052125 (2015).
- [62] J. Gonzalez-Ayala, A. Calvo Hernández, and J. M. M. Roco, From maximum power to a trade-off optimization of low-dissipation heat engines: Influence of control parameters and the role of entropy generation, *Phys. Rev. E* **95**, 022131 (2017).
- [63] Y. H. Ma, D. Xu, H. Dong, and C. P. Sun, Universal constraint for efficiency and power of a low-dissipation heat engine, *Phys. Rev. E* **98**, 042112 (2018).
- [64] K. Sekimoto and S. Sasa, Complementarity relation for irreversible process derived from stochastic energetics, *J. Phys. Soc. Jpn.* **66**, 3326 (1997).
- [65] Y. Izumida and K. Okuda, Efficiency at maximum power of minimally nonlinear irreversible heat engines, *Europhys. Lett.* **97**, 10004 (2012).
- [66] R. Long, Z. Liu, and W. Liu, Performance optimization of minimally nonlinear irreversible heat engines and refrigerators under a trade-off figure of merit, *Phys. Rev. E* **89**, 062119 (2014).
- [67] Z. C. Tu, Stochastic heat engine with the consideration of inertial effects and shortcuts to adiabaticity, *Phys. Rev. E* **89**, 052148 (2014).
- [68] V. Holubec, An exactly solvable model of a stochastic heat engine: Optimization of power, power fluctuations and efficiency, *J. Stat. Mech.* (2014) P05022.
- [69] P. R. Zulkowski and M. R. DeWeese, Optimal protocols for slowly driven quantum systems, *Phys. Rev. E* **92**, 032113 (2015).
- [70] J. Gonzalez-Ayala, J. M. M. Roco, A. Medina, and A. Calvo Hernández, Carnot-like heat engines versus low-dissipation models, *Entropy* **19**, 182 (2017).
- [71] R. S. Johal, Heat engines at optimal power: Low-dissipation versus endoreversible model, *Phys. Rev. E* **96**, 012151 (2017).
- [72] V. Singh and R. S. Johal, Feynman-Smoluchowski engine at high temperatures and the role of the constraints, *J. Stat. Mech.* (2018) 073205.
- [73] V. Blickle and C. Bechinger, Realization of a micrometre-sized stochastic heat engine, *Nat. Phys.* **8**, 143 (2012).
- [74] I. A. Martínez, É. Roldán, L. Dinis, D. Petrov, J. M. R. Parrondo, and R. A. Rica, Brownian Carnot engine, *Nat. Phys.* **12**, 67 (2015).
- [75] T. Shinjo, T. Okuno, R. Hassdorf, K. Shigeto, and T. Ono, Magnetic vortex core observation in circular dots of permalloy, *Science* **289**, 930 (2000).
- [76] G. Hrkac, P. S. Keatley, M. T. Bryan, and K. Butler, Magnetic vortex oscillators, *J. Phys. D: Appl. Phys.* **48**, 453001 (2015).
- [77] J. Gonzalez-Ayala, J. Guo, A. Medina, J. M. M. Roco, and A. Calvo Hernández, Energetic self-optimization induced by stability in low-dissipation heat engines (unpublished).
- [78] J. Gonzalez-Ayala, J. M. M. Roco, A. Medina, and A. Calvo Hernández, Entropy generation and unified optimization of Carnot-like and low-dissipation refrigerators, *Phys. Rev. E* **97**, 022139 (2018).
- [79] K. Deb, *Multi-objective Optimization Using Evolutionary Algorithms* (John Wiley & Sons, Inc., New York, 2001).
- [80] S. Sánchez-Orgaz, M. Pedemonte, P. Ezzatti, P. L. Curto-Risso, A. Medina, and A. Calvo Hernández, Multi-objective optimization of a multi-step solar-driven Brayton plant, *Energy Conv. Manage.* **99**, 346 (2015).
- [81] S. Kullback and R. A. Leibler, On information and sufficiency, *Ann. Math. Statist.* **22**, 79 (1951).
- [82] S. H. Strogatz, *Nonlinear Dynamics and Chaos: With Applications to Physics, Biology, Chemistry, and Engineering* (Westview Press, Boulder, CO, 2014).
- [83] P. E. Kloeden and E. Platen, *Numerical Solution of Stochastic Differential Equations* (Springer, Berlin, 1992).
- [84] W. N. Venables and B. D. Ripley, *Modern Applied Statistics with S* (Springer-Verlag, New York, 2002).
- [85] J. L. England, Dissipative adaptation in driven self-assembly, *Nat. Nanotechnol.* **10**, 919 (2015).
- [86] M. K. Belete and G. Balázsi, Optimality and adaptation of phenotypically switching cells in fluctuating environments, *Phys. Rev. E* **92**, 062716 (2015).
- [87] N. Perunov, R. A. Marsland, and J. L. England, Statistical Physics of Adaptation, *Phys. Rev. X* **6**, 021036 (2016).
- [88] R. Rao and M. Esposito, Nonequilibrium Thermodynamics of Chemical Reaction Networks: Wisdom from Stochastic Thermodynamics, *Phys. Rev. X* **6**, 041064 (2016).
- [89] T. J. Kobayashi and Y. Sughiyama, Stochastic and information-thermodynamic structures of population dynamics in a fluctuating environment, *Phys. Rev. E* **96**, 012402 (2017).
- [90] T. E. Ouldridge, C. C. Govern, and P. R. ten Wolde, Thermodynamics of Computational Copying in Biochemical Systems, *Phys. Rev. X* **7**, 021004 (2017).
- [91] D. Helbing and T. Vicsek, Optimal self-organization, *New J. Phys.* **1**, 13 (1999).